BioChip Journal (2024) 18:115–136
https://doi.org/10.1007/s13206-023-00135-x

ORIGINAL ARTICLE

Numerical-Simulation-Based Buffer Design for Microchip Electrophoresis with Capacitively Coupled Contactless Conductivity Detection

Jianyun Meng[1] · Nebiyu Getachew Arega[1] · Bhargav Krishna Pullagura[1] · Dohyun Kim[1]

Received: 18 September 2023 / Revised: 23 November 2023 / Accepted: 24 November 2023 / Published online: 3 January 2024

Abstract
We present a numerical simulation method for designing a buffer system in microchip electrophoresis (MCE) equipped with capacitively-coupled-contactless-conductivity detection (C4D). One of the key design considerations for MCE-C4D is background electrolyte (BGE). This is because a C4D typically exhibits low sensitivity, and optimizing BGE conditions (e.g., base and acid species, pH, and ionic strength) can improve its sensitivity. However, BGE has been traditionally designed through experience or trial and error, which is time- and reagent-consuming. In this study, we employ Simul 5, an open-source electrophoresis simulation software, for rational BGE design. Four BGEs including trimethylamine (TEA)/acetic acid (AcOH, pH 10.6), MES/His (pH 6.1), MES/TRIS (pH 8.1), and TRIS/HCl (pH 7.4), previously used in electrophoresis-C4D of amino acids and protein, were selected for evaluation of our numerical method. Glutamic acid (Glu) was selected as a model analyte for initial simulation verification. Our numerical simulation revealed that the best achievable detection sensitivity was 1.046×10^{-5} S/(m μM) in the TRIS/HCl buffer because anionic Glu species with a low mobility (27×10^{-9} m^2/Vs) replaced Cl^- co-ion of a high mobility (79.1×10^{-9} m^2/Vs) in the analyte zone, leading to a significant negative conductivity peak. TEA/AcOH, MES/His, and MES/TRIS buffers exhibited progressively lower sensitivity. After the initial evaluation, trypsin inhibitor (TI), a more complex proteinous analyte was tested in the MES/His and MES/TRIS BGEs. The best detection sensitivity was 1.032×10^{-4} S/(m μM) in the MES/TRIS buffer because counter-ionic species $TRIS^+$ of a high mobility (29.5×10^{-9} m^2/Vs) was replaced by the ionic TI, characterized by a large charge (− 11.5) and a low mobility (8.08×10^{-9} m^2/Vs), resulting in a strong negative peak. Based on a comprehensive analysis of the impacts of compositional changes in each ionic species of the analyte zone on conductivity-peak height, we propose a BGE design guideline for enhanced sensitivity. Subsequent MCE-C4D confirmation experiments demonstrated excellent qualitative agreement with the simulation results for the Glu and TI analytes. We anticipate that our numerical analysis method will find wide application in designing BGEs for portable MCE-C4D systems by enhancing sensitivity.

Keywords Microchip electrophoresis (MCE) · Capacitively coupled contactless conductivity detection (C4D) · Background electrolyte (BGE) · Buffer system design · Simul 5 · Glutamic acid · Trypsin inhibitor

1 Introduction

Microchip electrophoresis (MCE) emerged as an early technology driver in the microfluidics field [1]. In contrast to conventional capillary electrophoresis (CE) relying on single or bundled glass or quartz capillaries, MCE uses photolithographically-defined networks of capillaries (i.e., microfluidic channels). This invention has unlocked opportunities for high-throughput, massively parallel, and multi-step electrophoretic assays [2]. Compared to CE, MCE devices feature shorter channels and higher electric fields due to effective heat dissipation, allowing for faster separation while maintaining comparable resolution [3]. MCE has been applied for the separation and detection of diverse charged species including organic [4] and inorganic ions [5], nucleic acids [6], amino acids [7], peptides [8], proteins [9], nanoparticles [10], and even non-ionic species through

✉ Dohyun Kim
dohyun.kim@mju.ac.kr

[1] Department of Mechanical Engineering, Myongji University, 116 Myongji-ro, Yongin 17058, Republic of Korea

adaptations like microchip micellar electrokinetic chromatography (MCMEKC) [11].

Fluorescence measurement stands as one of the most frequently employed techniques in MCE due to its excellent limit of detection (LOD) in the sub-nM range [12]. However, fluorescent detection requires laborious labeling of fluorescence tags. Moreover, labeling the target analyte may induce conformational change, thereby altering its mobility, functions, and binding affinity with partnering molecules [13]. Complex and bulky optical components and instrumentation for fluorescence detection pose a major barrier to the widespread adoption of the MCE in a compact format for point-of-care (POC) applications [14].

In contrast, conductivity detection is a universal and label-free detection technique, enabling the quantification of charged analytes without the need for fluorescence-probe tagging [15–18]. The electronics-only detection system [16, 19, 20] can be miniaturized using integrated circuits [21], facilitating the realization of a compact and portable analytical instrument. Conductivity detection can be implemented in either contact [15] or contactless mode [22]. In the contact mode, detection electrodes directly interact with the electrophoresis buffer, inducing electrochemical side effects such as electrolysis [14], electroactive species reduction or oxidation [23], electrode passivation [24], and interference from high separation voltages [25]. Furthermore, incorporating electrodes inside a microchannel poses a challenge in microfabrication [24]. In the contactless mode, conversely, electrodes remain electrically isolated from the solution, circumventing the aforementioned artifacts. Analytes are detected through capacitive coupling in the capacitively coupled contactless detection (C4D) mode, a dominant contactless method [26]. Several commercial detectors, including ones from eDAQ, TraceDec, and ADMET, are already available [27]. Moreover, the fabrication process is simpler because electrodes can be patterned on the chip surface after microfluidic chip manufacturing [28] or external electrodes can be pressed onto the chip surface using a clamp [29]. Given these advantages, C4D has been applied in MCE for various analytes [30] including inorganic ions [31], organic ions [32], amino acids [3], peptides [33], proteins [34], DNA [35], cells [36], and even liquid droplets [37].

Nevertheless, a critical shortcoming of C4D lies in its inferior LOD, compared to that of fluorescent detection (e.g., ~ 10 μM range [3] vs. ~ 1 pM range for amino acid [38]). The major reasons are weak capacitive coupling with the solution and strong stray coupling between the excitation and sensing electrodes [29]. Notably, the low coupling capacitance with the solution (10^{-15}–10^{-13} F range) leads to increased impedance and subsequent reduction of analytical signals [39–41]. Coupling capacitance can be enhanced by diminishing the channel-lid thickness [25] and/or employing a lid material with a high dielectric constant [42]. However, the thickness cannot be reduced excessively due to fragility. Furthermore, the dielectric constants of chemically and mechanically stable, transparent lid materials are limited to a 2−4 range (e.g., glass, quartz, and thermoplastics). The stray capacitance between excitation and sending electrodes typically surpasses the coupling capacitance [29, 39]. Consequently, the stray capacitor exhibits low impedance, thereby causing signal loss through this pathway and ultimately reducing analytical signal. There have been attempts to reduce stray capacitance by increasing the gap between the electrodes, but separation resolution has suffered as a result [43]. In an alternative approach, a grounded faradaic shield (e.g., metal foil) has been placed between the two electrodes to diminish stray coupling in MCE [41]. However, implementing a vertical faradaic shield around a horizontal microchannel poses a challenge, and the faradaic shield in MCE is not as effective as in CE [44]. Alternatively, grounded horizontal electrodes are proposed for MCE [29], but this has been met with limited success while adding complexity to the detection system. Sample preconcentration methods including field amplified sample stacking (FASS) [45], isoelectric focusing (IEF) [14], and isotachophoresis (ITP) [46] have also been employed in MCE-C4D. However, the chip and assay designs were complicated.

Background electrolyte (BGE) is a crucial component of an electrophoresis system. Comprising acids, bases, and/or salts, BGE carries a current when subjected to separation electric field. Essentially it functions as a buffer, maintaining a consistent solution environment for the migrating analytes regardless of the sample composition and running conditions [47]. The pH is a critical parameter of the BGE that demands stability during electrophoresis due to its influence on ionization, hence net charge, and consequently the apparent mobility of analytes [48]. To achieve good performance, conductivity should be kept low so that a significant portion of the current is delivered by analytes. Otherwise, the analytes will migrate at an unacceptably low speed. Additionally, low currents reduced Joule heating, thereby preventing undesirable zone dispersion [49] and detector baseline drift [39]. Therefore, weak acids and/or bases of low mobility are traditionally chosen. Analyte ions within a zone also influence local conductivity. A C4D, or any conductivity detector, measures the conductivity change $\Delta\kappa$ between the blank BGE and the analyte zone (or conductivity-peak height). This $\Delta\kappa$ is not only a function of analyte species and concentrations but also depends on BGE composition and pH. Consequently, C4D sensitivity is strongly influenced by the BGE. Therefore, designing an appropriate BGE is important for improving sensitivity and LOD [50–52].

BGEs for C4D are usually designed by experience or trial-and-error, augmented by empirical investigations [50, 53–55]. Although some design rules have been suggested [49], the emphasis in many cases has been primarily on

improving separation resolution rather than LOD [53]. For instance, when seeking to improve the separation resolution and LOD of biogenic amines, candidate combinations of buffering species such as MES-His, HEPES-His, Tris-His, CHES-His, and CAPS-His, were assessed to select the optimal combination, HEPES-His. Secondly, five different compositions of the HEPES-His buffer (with a total concentration of 50 mM) were tested, determining the best 5:1 ratio. Thirdly, the overall ionic strength was varied while maintaining the ratio, with a twofold increase being chosen (50 mM HEPES and 10 mM His). Lastly, the ratio was again adjusted to 5:1, 10:1, and 20:1 while keeping the HEPES concentration to 50 mM, yielding the final composition of 10:1 [50]. However, adopting such empirical approaches would consume substantial time and reagents. Recognizing this, a more systematic approach, the design of experiment (DOE), has been applied in optimizing BGE concentration and pH for the separation of tobramycin. Nonetheless, this approach lacks a mechanistic understanding of how these parameters impact separation resolution and conductivity-peak height [51].

A mathematical-model-based rational design can be a more accurate, time- and cost-effective approach. The electrophoresis models can make highly precise predictions with accurate electrokinetic parameters of ionic species [56]. The models can also elucidate how BGE conditions impact key electrophoresis results in a CE-C4D system [57]. A theoretical model was introduced to find a BGE composition for increased $\Delta\kappa$ and signal-to-noise ratio (SNR). This model relies on Kohlrausch regulating function (KRF) along with the mobilities of BGE co-ion and counter-ions as well as analyte ions [15, 58]. While the theoretical model provides a first-degree guideline for BGE design, it is limited due to the assumption of fully-dissociated, monovalent species [59]. An alternative approache that builds upon a modified KRF have considered weak monovalent electrolytes and a BGE of neutral pH (ranging from 4.5 to 9.5) where the contributions of OH^- and H^+ ions are negligible [60]. Subsequent improvements have incorporated consideration for multivalent ions and the pH beyond the neutral regions. Gaš et al. suggested coupled algebraic equations based on electroneutrality equation, mass-balance equation, acid–base equilibria, and Ohm's law along with their numerical calculation for BGE optimization [60]. This model has also predicted electromigration dispersion and conductivity detector response (e.g., sensitivity). An improved model from the same research group incorporated the dependency of mobility and acid–base equilibria on concentration and predicted time-dependent conductivity signals [61]. However, the model overlooked the diffusive dispersion of ionic species in zones, restricted the number of BGE and analyte species (total of 5), and did not elucidate time- and position-dependent concentration profiles [60, 61]. Therefore, more accurate models are demanded, particularly to analyze electrophoresis features that reflect real-world situations more closely, where (1) all ionic species are multivalent and partially dissociable including macromolecules like proteins, (2) the numbers of BGE co-ions/counter-ions and analyte ions are unrestricted, (3) diffusive dispersion of analyte ions are considered, and (4) time- and position-dependent information regarding electrophoresis phenomena are predicted [59].

Consequently, more rigorous mathematical models for electrophoresis have been developed, along with simulation software based on these models. Gaš [62, 63], Bier [57], Santiago [64], and Moser and Thorman [65] have created simulation models to investigate various electrokinetic phenomena, including capillary zone electrophoresis (CZE) [66], ITP [67], IEF [14], and electrokinetic chromatography (EKC) [68]. These efforts led to the development of dynamic simulation software [66] such as Gentrans [57], Simul [63], PeakMaster [61], and Spresso [64]. Detailed spatial and temporal electrophoresis information including analyte and BGE concentrations, conductivity, electric field, pH, and current can be acquired from the software. Among the mentioned software options, PeakMaster and Simul have been employed most widely [66].

PeakMaster has contributed to the design of BGEs [52–54, 61]. However, its primary applications have been predicting elution order and separation performance [52, 66], estimating the mobilities of analytes and system peaks [49], as well as pre-evaluating electromigration dispersion [54, 61] and conductivity-detection response [61]. The operational principle of PeakMaster involves a linearized approximation of the complex nonlinear governing equation of electrophoresis [66]. As a result, although PeakMaster offers faster execution, its solutions are less accurate than those provided by Simul [66]. In this context, we embark on exploiting Simul software version 5 (i.e., Simul 5), in order to (1) comprehensively explore the impact of each BGE component on the sensitivity of an MCE-C4D, and (2) provide a design guideline for BGE compositions that maximize sensitivity. The time- and position-dependent mass-balance equation, electroneutrality equation, acid–base equilibria, and Ohm's law serve as the foundation for Simul 5. This model incorporates adjustments to ion mobilities following the Onsager–Fuoss and the Debye–Hückel theories to calculate the activities of ionic species.

In this study, we opted for glutamic acid (Glu) and trypsin inhibitor (TI) as model analytes. Amino acids (AAs) are the building blocks of protein. Therefore, the analysis of AAs holds significance in clinical, food, and environmental sciences. Conductivity detection is a label-free method favored for CE-separated AAs over UV spectroscopy, which exhibits lower sensitivity [3, 54, 55]. C4D detection of AAs has proven successful because of their high charge-to-mass ratio

attributed to at least two ionizable amine and carboxylic groups coupled with a small molecular mass of 75–204 Da [3, 30, 54, 55]. Among the AAs, Glu was selected as a model analyte because a sensitive C4D detection is possible due to full ionization (isoelectric point = 3.2) at the tested pH range (6.1–10.6). Moreover, Glu holds significance in medicine because it is the most abundant excitatory neurotransmitter in the vertebrate nervous system [69]. Additionally, MCE-C4D has demonstrated protein analysis including human serum albumin, human transferrin [34], immunoglobulin M [70], lysozyme, TI [71], cytochrome c, myoglobin [72], ribonuclease, β-lactoglobulin, α-lactalbumin [73], immunoglobulin G (IgG) [30], hemoglobin, and catalase [74]. The typical LOD for proteins ranges from 0.1 to 10 μM, occasionally reaching 100–1 nM range [30, 70, 74]. We employed TI as a model analyte because it is a serine protease inhibitor with unique physiological functions encompassing anti-cancer, anti-inflammatory, anti-bacterial, and satiety qualities [75]. In addition, the TI is often used in developing electrophoresis assays due to its affordability and usefulness as an internal standard [76].

As shown in Fig. 1, our BGE design process is as follows: (1) select model BGEs (e.g., a binary BGE with a weak acid and base or salt) which are simple yet commonly used in CE-C4D for AAs and protein detection; (2) run numerical simulations with Glu and TI using Simul 5; (3) analyze changes in concentrations of ionic species (analyte, BGE co-/counter-ions) from the blank BGE to the analyte zone, elucidating their contribution to $\Delta\kappa$; (4) establish a rational design guideline for BGEs for an enhanced C4D sensitivity; (5) run numerical simulations with varying concentration of Glu and TI; (6) establish the relationship between concentrations of analytes and $\Delta\kappa$; (7) select the optimal BGE for each analyte (Glu and TI) based on their respective sensitivity; (8) validate simulation results with experimental verification; and lastly (9) design new, improved BGEs with the aid of the established design guideline and return to the step (5) for design iteration if further improvement is required. In this work, steps (1) – (8) will be described.

2 Experimental and Simulation

2.1 Materials and Reagents

2-hydroxyethyl cellulose (HEC), 2-(N-morpholino)ethanesulfonic acid (MES), Tris(hydroxymethyl)aminomethane (TRIS), acetic acid (AcOH), triethylamine (TEA), L-glutamic acid (Glu), L-histidine (His), and trypsin inhibitor (TI) were purchased from Sigma-Aldrich (St. Louis, Missouri, United States). Alexa Fluor 568 Antibody Labeling Kits were purchased from Thermo Fisher Scientific (Waltham, MA, United States). A 1-N Sodium hydroxide (NaOH) solution was purchased from Deajung Chemicals (Siheung, South Korea), and a 1-N TRIS/HCl solution was obtained from Dynebio (Geongji Do, South Korea). Deionized (DI) water with a resistivity of 18.2 MΩ was processed using Pure Power II made by Human Corp (Seoul, South Korea).

2.2 Instrumentation and Data Acquisition

The C4D system, depicted in Fig. 2, comprises an ER-225 conductivity detector, an ET-121 C4D headstage for securing and connecting a microfluidic chip, and PowerChrom software responsible for electronics control. This C4D system was sourced from eDAQ (Denistone, Australia). In the C4D system, a high-frequency AC voltage signal is generated by one of the gold-coated copper electrodes, and the resulting AC current is detected by the other electrode. Subsequently, this output AC current is converted and amplified to an AC voltage signal through a trans-impedance amplifier. Then, offset and noise are removed. The adjustable input AC voltage amplitude ranges from 2 to 200 V, and the input frequency ranges from 50 to 1260 kHz. Amplitude and

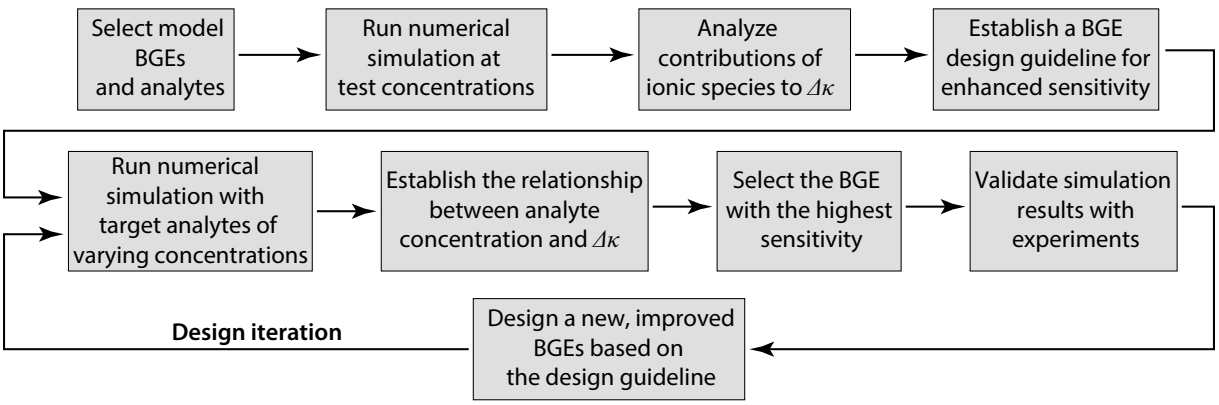

Fig. 1 Design process for a BGE for MCE-C4D based on numerical simulation using Simul 5 software

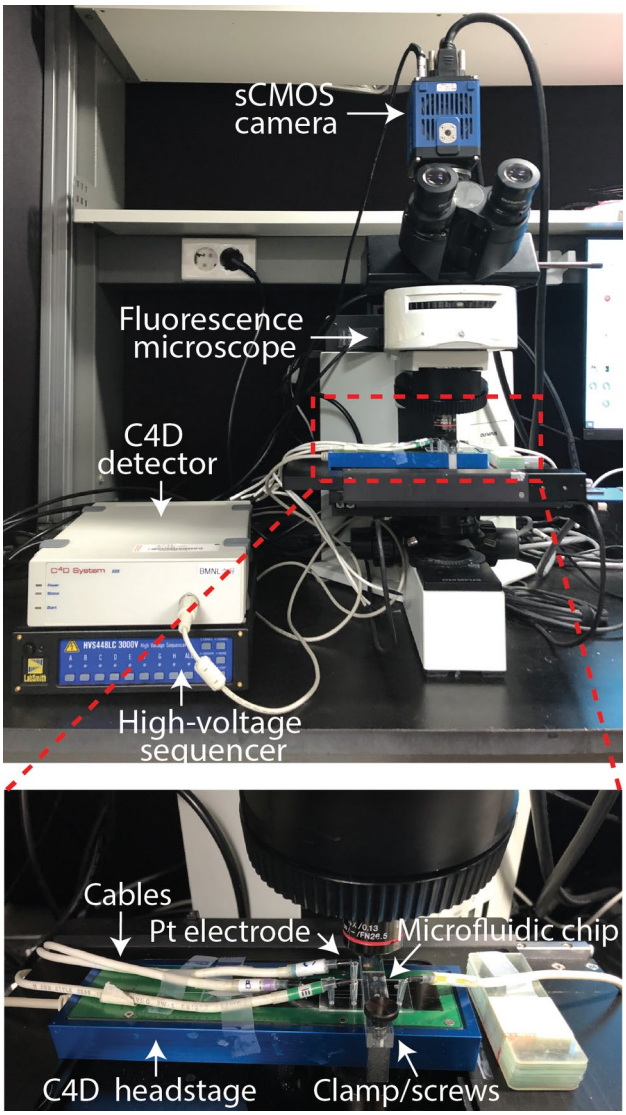

Fig. 2 Microchip electrophoresis (MCE) set-up. A high-voltage sequencer controls electric fields inside microchannels. An epi-fluorescence microscope, equipped with a high-speed sCMOS camera and a wide-band LED light source, was employed to capture fluorescence images. A C4D detector measures and records the conductivity signal generated from the microchip, which is placed on the microscope stage via a C4D headstage. The inset figure illustrates a glass microchip securely clamped on the headstage and connected to the high-voltage sequencer via platinum electrodes and lead wires

frequency must be optimized for maximum C4D sensitivity using a standard solution because the coupling capacitance C_{cl} changes each time a microfluidic chip is clamped to the C4D stage (see inset figure).

The loading and separation processes in MCE are driven by a high-voltage sequencer (HVS448LC, LabSmith, Livermore, CA, United States). Four platinum electrodes (Nialco, Tokyo, Japan) are employed to execute a voltage program in a double-T junction microfluidic chip. Fluorescence signals are recorded by an epi-fluorescence upright microscope BX50 (Olympus, Tokyo, Japan), equipped with an sCMOS camera (PCO.edge 5.5 M, PCO Imaging, Kelheim, Germany) and a wide-band LED light source (pE300 ultra, CoolLED, Andover, United Kingdom). MetaMorph (Molecular Devices, San Jose, CA, United States), an image acquisition and analysis software, controls all electrophoresis hardware. Electropherograms in terms of fluorescence intensity are generated using ImageJ (National Institutes of Health, Bethesda, MD, United States) after importing image stacks recorded via MetaMorph.

A double-T junction glass microfluidic chip exhibited in Fig. S1a in Supplementary Information (SI) was fabricated using a foundry service (Perkin Elmer, Waltham, MA, United States). To enhance C_{cl}, the chip was fabricated in a specialized thin glass substrate (300 µm soda-lime glass). The bottom lid thickness was 250 µm because the etch depth was 50 µm. The four channels have varying lengths of 0.575, 1.375, 1.375, and 3.275 cm, respectively. Although the nominal channel width is 50 µm, isotropic wet etching results in a top channel width of 150 µm.

2.3 Protein Labeling

For cross-confirmation of C4D protein detection via fluorescence imaging, TI was labeled using the Alexa Fluor 568 Antibody Labeling Kit, following the manufacturer's instructions with slight modifications. Briefly, 100 mg of TI was dissolved in 100 µL 1 × PBS buffer, and then 8.4 µL of the dye solution (11.3×10^{-2} M) was added. The solution was placed in a dark environment at room temperature for 1 h with vortexing every 30 min. After labeling, protein purification and buffer exchange were conducted using a centrifuge (5810R, Eppendorf, Hamburg, Germany) and a Bio-Spin 6 column (Bio-Rad, Hercules, CA, United States). If the concentration of purified TI was unacceptably low, a 10 kDa centrifuge filter (Amicon Ultra-15, Millipore, Burlington, MA, United States) was used to concentrate the diluted TI samples.

2.4 Microchip Electrophoresis Procedure

A standard two-step double-T junction MCE process was adopted to incorporate on-stage C4D detection [14, 77]. The MCE procedure comprises the following three steps.

Step 1: Microfluidic chip installation on headstage.

The microfluidic chip is clamped on the headstage. The chip's bottom lid makes hard contact with the electrodes fabricated on a printed circuit board (PCB), using a custom-made PMMA (polymethyl methacrylate) clamp. The clamp presses and holds the chip firmly against the PCB using screws. The clamp includes a window in the center to enable distortion-free optical monitoring of fluorescence-labeled

analytes. The PCB area around the clamping region is marked in black to minimize light reflection from the gold electrodes and background autofluorescence from the PCB. It is crucial to avoid touching the chip once clamped, because even a slight impact can alter C_{cl} and cause a dramatic change in the C4D signal.

Step 2: Microchannel cleaning.

After chip installation, a 1-N sodium hydroxide solution is employed to wash the microchannels for 10 min using a suction pump (BF-101, BioFree, Bucheon, South Korea). Subsequently, the microchannels are rinsed with DI water for an additional 10 min. Then the channels are rinsed with a chosen BGE solution for another 10 min to establish a stable conductivity baseline. Finally, the channels are filled with the same BGE for AA analysis. For TI analysis, 2% HEC is added to BGEs for suppressing electroosmotic flow (EOF). Without the viscous medium, achieving proper injection and separation of the protein was challenging. During the cleaning process, care must be taken to avoid unnecessary contact with the chip.

Step 3: Electrophoretic sample loading, separation, and detection.

After microchannel cleaning, reservoirs made from modified micropipette tips (200 µL) are fitted to the four wells (S: sample well, SW: sample-waste well, B: buffer well, BW: buffer-waste well) to contain BGE and sample solutions (Fig. S1a in SI). An analyte sample (Glu or TI dissolved in the chosen BGE) is loaded into the S well using a micropipette, and the BGE is added to the remaining three wells. An electric field of 83.14 V/cm (137.3 V/cm for protein) is applied between S and SW to load the sample for 30 min (Fig. S1b). The loading time was empirically determined for Glu as the loading process of unlabeled Glu over the double-T junction cannot be monitored. Subsequently, a separation electric field of 283.66 V/cm is applied for 10 min between the junction and BW to form an analyte zone and to transfer the zone towards the BW (Fig. S1c). Pull-back electric fields for a "pinched injection" are also applied between the junction and S and between the junction and SW to create a sharp analyte zone. The C4D detector continuously monitors the conductivity signal during migration and detects the analyte in the form of a conductivity peak when the sample zone passes through the detection area located between the two C4D electrodes. Glu was unlabeled and thus only able to be monitored via a conductivity signal because fluorescent labeling significantly alters electrophoretic properties. For TI measurement, the sCMOS camera simultaneously records fluorescent images at the detection area. Capturing fluorescence images is essential for identifying a TI peak amid unidentified system conductivity peaks (Section S.1 in SI) [49]. Optimization of loading and separation processes, including the choice of viscous medium (i.e., 2% HEC solution), is also performed using fluorescence imaging. Again, it is crucial to minimize contact with the chip to ensure reproducible measurement throughout the electrophoresis procedure.

2.5 Running Electrophoresis Simulation on Simul 5

Simul 5 is an open-source electrophoresis simulation software (Fig. 3) [63]. It operates on a 1-D migration of ionic species under an electric field (i.e., considers only the axial direction within a capillary) as shown in Fig. S3 of SI. The mathematical model incorporates the 1-D transport equation (or mass-conservation equation), Ohm's law, acid–base equilibria, charge-neutrality condition, Onsager-Fuoss theory, and Debye–Hückel theory. Details of these governing equations are given in Section S.1 of SI. Simul 5 solves the coupled nonlinear equations numerically, yielding more precise numerical solutions, a contrast to the linearized, approximated solutions offered by PeakMaster [63].

In Simul 5, various input parameters can be specified: (1) geometric factors including capillary length (l) and diameter, alongside the positions of injection and detection sites; (2) compositions of both the BGE and analyte species, including proteins; and (3) operating conditions encompassing separation voltage, temperature, simulation time, injected sample size, and EOF mobility. Conditions for numerical simulation such as time step (Δt), mesh number (n), and maximum numerical error $|\varepsilon_{max}|$ can also be adjusted to achieve a balance between numerical-solution accuracy and speed. The software affords real-time visualization of time- and position-dependent electrophoretic behaviors such as constituent concentrations, conductivity, electric field, pH, and ionic strength. These data can also be exported in text files for further analysis. Users are only required to specify the concentrations of ionic constituents because Simul 5 contains the database of mobilities and acid dissociation constants (pK_a) for commonly used ionic species. A comprehensive workflow is detailed in Section S.3 of SI.

A set of nonlinear equations (Eq. S1–S7 in SI) are solved using the finite-difference, Runge–Kutta, and predictor–corrector methods [63]. Like other numerical methods, the time step (Δt) and mesh size (i.e., $\Delta x = l/n$) are critical parameters affecting the convergency and accuracy of numerical solutions. Accuracy usually improves with decreasing Δt and Δx until round-off error dominates. However, excessively small Δt and Δx are impractical because computation time and memory usage will become unmanageable. Furthermore, we observed that numerical accuracy and convergency correlate with the composition of ionic constituents. Therefore, optimal pairs of (Δt, n) for each model BGEs and each analyte (Glu or TI) were determined by varying Δt from 0.01 to 0.00005 s and n from 20 to 10,000 to minimize numerical error |ε| (Fig. S7 and S9). The detailed optimization procedure is outlined in Section S.4 of SI. Optimized simulation conditions for Glu and TI are provided in Tables S2 and S3.

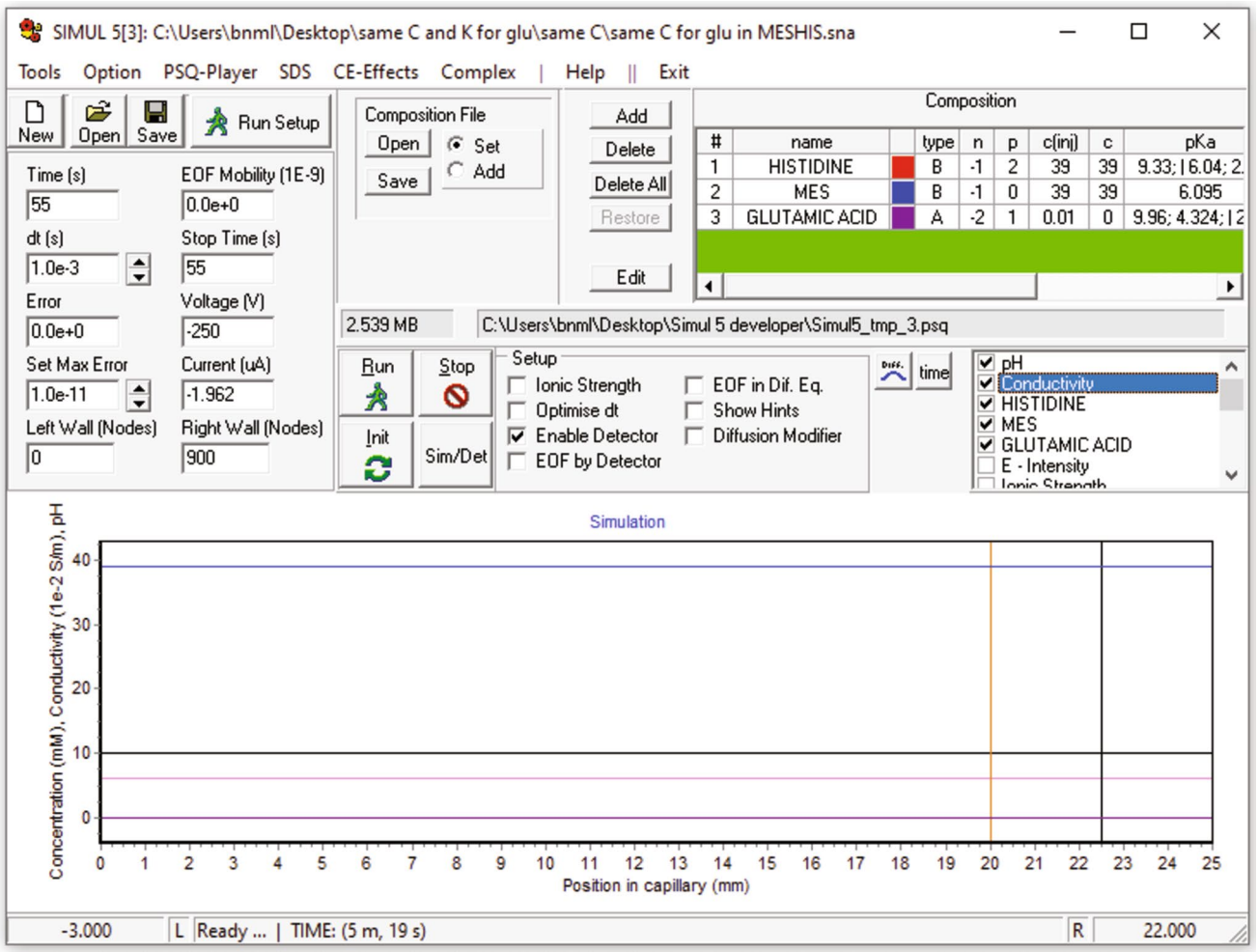

Fig. 3 Simul 5 (Simul version 5), an open-source electrophoresis software developed by Gaš et al. [63]

2.6 Selection of Model Background Electrolytes and Analytes for Electrophoresis Simulation

We selected four BGEs previously employed in CE-C4D for AAs and/or proteins as the model buffer systems: (1) TEA/AcOH at pH 10.6 [72], (2) MES/His at pH 6.1 [34], (3) TRIS/MES at pH 8.1 [78], and (4) TRIS/HCl (pH 7.4) buffers [70]. Although more acidic buffers (e.g., AcOH at pH 2.2 [55] and benzoic acid at pH 3.1) and strongly alkaline buffers (TEA at pH 11.3 [79]) have also been employed, we confined our selection to a milder pH range of 6.1–10.6. Primarily, these BGEs are intended for use in electrophoretic immunoassays where the buffer cannot be significantly acidic (i.e., below pH 4) to maintain binding affinity [80]. Additionally, these BGEs will be employed in polyacrylamide gel electrophoresis in the future [81]. Excessively alkaline buffer should be avoided because it can lead to polyacrylamide hydrolysis [76]. An amino-acid Glu and protein trypsin inhibitor (TI) were chosen as model analytes.

3 Results and Discussion

3.1 Electrophoresis Simulation of Glutamic Acid

3.1.1 Time- and Position-Dependent Concentration of Analyte and Corresponding Conductivity Peak

Using the optimized simulation conditions (Section S.4), electrophoresis simulation of Glu was conducted in the four selected BGEs. As an initial exploration of using Simul 5 for BGE design, we examined the migration behavior of a 0.01 mM Glu analyte zone in the TRIS/HCl buffer at pH 7.4 and the co-migrating conductivity peak. Figure 4a illustrates the time evolution (0, 15, 30, 45, and 60 s) of the electrophoretic migrations of Glu (black line) under an electric field of 100 V/cm, along with the corresponding conductivity κ (blue line).

The initial profile of the injected sample was Gaussian-like with a flat top. The peak shape was defined by two

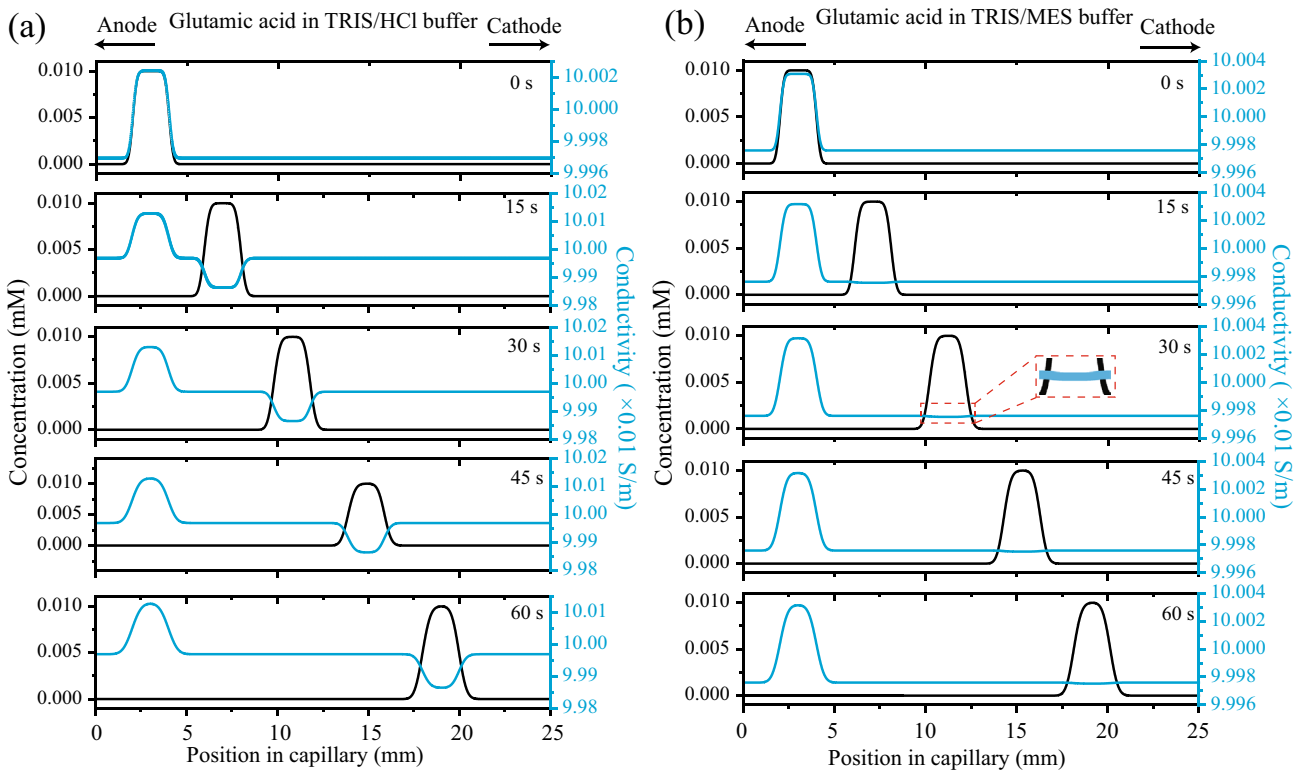

Fig. 4 Time sequences of electrophoresis simulation conducted for glutamic acid (Glu) in (**a**) TRIS/HCl buffer and (**b**) TRIS/MES buffer. Analyte zone of Glu (black line) and resulting conductivity peaks (blue line) are depicted for each time step of 0, 15, 30, 45, and 60 s. Both cases exhibited negative conductivity peaks but in a significantly smaller magnitude for the TRIS/MES case (inset of the 30 s case). Electrophoresis condition: Glu concentration = 10 μM, simulation time = 60 s, capillary length = 25 mm, and separation electric field = 100 V/cm

parameters in Simul 5 (Section S.3): Peak width = 2 mm and Peak edge width = 0.5 mm. Its initial position at $t = 0$ s was defined by the parameter "Injection site" (3 mm). The Glu zone dispersed due to diffusion as migrating downstream, gradually forming a Gaussian peak shape. The diffusion coefficients in Simul 5 are estimated using the Nernst-Einstein relation [82]. Over time, the peak width increased by 33% while the peak height decreased by 0.05% at 60 s due to the diffusive dispersion. We observed two conductivity peaks during the simulation. The first conductivity peak tracked the migrating Glu zone. This peak exhibited a negative value (i.e., negative peak), indicating reduced conductivity in the analyte zone compared to the neighboring BGE. This phenomenon resulted from the displacement of high-mobility Cl^- ions in the BGE by the low-mobility ionic Glu accumulated in the zone (further elaborated in the next section). The second conductivity peak remained at the injection site. This peak appeared because the Cl^- and $TRIS^+$ ions displaced from the analyte zone were collected at this injection site [83].

Another simulation was conducted to investigate Glu migration in the TRIS/MES buffer at pH 8.1 (Fig. 4b). A similar relationship was observed between the injected and migrating analyte peaks, as well as between immobile and mobile conductivity peaks. The migrating analyte zone also led to a negative conductivity peak, albeit with a significantly smaller magnitude (inset of Fig. 4b). This diminished peak height is primarily because the increase in conductivity caused by the enriched Glu was mostly counteracted by the decrease in conductivity resulting from the displaced MES^- and $TRIS^+$ ions from the same zone (see the next section for details). Additionally, the results for the TEA/AcOH and MES/His BGEs are presented in Section S.5 of SI. The two cases exhibited positive peaks in contrast to the TRIS/MES and TRIS/HCl cases. The BGEs, ranked in order of the magnitude of the conductivity peak, denoted as $|\Delta\kappa|$, were TRIS/HCl, TEA/AcOH, MES/His, and TRIS/MES.

3.1.2 Influence of Ionic Concentration and Mobility on Conductivity of Analyte Zone

Using electrophoresis data at $t = 60$ s exported from Simul 5 (Fig. 4), we conducted a comprehensive analysis of the individual contributions of various ionic species to $\Delta\kappa$, the conductivity-peak height. This analysis aimed to facilitate the design of a buffer system that can maximize C4D sensitivity.

The analysis results for two BGEs are shown in Tables 1 and 2. These tables enumerate the concentrations of microforms of each ionic species at two positions: the center of the Glu analyte zone ("peak") and its shoulder ("baseline") where

Table 1 Concentrations of microforms of the BGE components, analyte, hydrogen, and hydroxide ions and their contribution to the peak-baseline conductivity change $\Delta\kappa$ for the glutamic acid (Glu) electrophoresis simulation in the TRIS/HCl buffer at pH 7.4. The concentrations and conductivity are evaluated at the center of the Glu zone ("Peak") and background electrolyte ("Baseline")

		Analyte			BGE		H^+/OH^-		Total
		Glu^{2-}	Glu^-	Glu^+	$TRIS^+$	Cl^-	H^+	OH^-	
Concentration (M)	Peak	2.75×10^{-8}	9.95×10^{-6}	4.55×10^{-14}	9.54×10^{-3}	9.52×10^{-3}	3.96×10^{-8}	2.52×10^{-7}	
	Baseline	0	0	0	9.54×10^{-3}	9.54×10^{-3}	3.97×10^{-8}	2.52×10^{-7}	
	Change	2.75×10^{-8}	9.95×10^{-6}	4.55×10^{-14}	-5.26×10^{-6}	-1.525×10^{-5}	-2.26×10^{-11}	1.439×10^{-10}	
	Relative change	100%	100%	100%	− 0.0551%	− 0.160%	− 0.0570%	0.0571%	
Conductivity (S/m)	Peak	2.88×10^{-7}	2.59×10^{-5}	1.258×10^{-13}	2.71×10^{-2}	7.27×10^{-2}	1.385×10^{-6}	4.99×10^{-6}	9.98×10^{-2}
	Peak contribution (%)	0.0003%	0.0259%	0.00%	27.2%	72.8%	0.0014%	0.0050%	100%
	Baseline	0	0	0	2.71×10^{-2}	7.28×10^{-2}	1.386×10^{-6}	4.99×10^{-6}	9.99×10^{-2}
	Baseline contribution (%)	0%	0%	0%	27.2%	72.8%	0.0014%	0.0050%	100%
	Contribution change (%)	0.0289%	2.59%	0.0000%	1.364%	− 3.99%	0.0001%	0.0008%	0.00%
	Conductivity change	2.88×10^{-7}	2.59×10^{-5}	1.258×10^{-13}	-1.495×10^{-5}	-1.164×10^{-4}	-7.91×10^{-10}	2.85×10^{-9}	-1.052×10^{-4}
	Relative change	− 0.274%	− 24.6%	0.00%	14.22%	110.7%	0.0008%	− 0.0027%	100.00%

Table 2 Concentrations of microforms of the BGE components, analyte, hydrogen, and hydroxide ions and their contribution to the peak-baseline conductivity change $\Delta\kappa$ for the glutamic acid (Glu) electrophoresis simulation in the TRIS/MES buffer at pH 8.1. The concentrations and conductivity are evaluated at the center of the Glu zone ("Peak") and background electrolyte ("Baseline")

		Analyte			BGE		H^+/OH^-		Total
		Glu^{2-}	Glu^-	Glu^+	$TRIS^+$	MES^-	H^+	OH^-	
Concentration (M)	Peak	1.313×10^{-7}	9.85×10^{-6}	1.940×10^{-15}	1.802×10^{-2}	1.801×10^{-2}	8.23×10^{-9}	1.215×10^{-6}	
	Baseline	0	0	0	1.802×10^{-2}	1.802×10^{-2}	8.23×10^{-9}	1.215×10^{-6}	
	Change	1.313×10^{-7}	9.85×10^{-6}	1.940×10^{-15}	-8.09×10^{-8}	-1.019×10^{-5}	-4.84×10^{-14}	7.15×10^{-12}	
	Relative change	100%	100%	100%	− 0.0004%	− 0.0566%	− 0.0006%	0.0006%	
Conductivity (S/m)	Peak	1.375×10^{-6}	2.57×10^{-5}	5.37×10^{-15}	5.13×10^{-2}	4.86×10^{-2}	2.88×10^{-7}	2.40×10^{-5}	9.99×10^{-2}
	Peak contribution (%)	0.0014%	0.026%	0.00%	51.3%	48.7%	0.00003%	0.024%	100%
	Baseline	0	0	0	5.13×10^{-2}	4.87×10^{-2}	2.88×10^{-7}	2.40×10^{-5}	9.99×10^{-2}
	Baseline contribution (%)	0.00%	0.00%	0.00%	51.3%	48.7%	0.00%	0.024%	100%
	Contribution change (%)	0.0014%	0.026%	0.00%	0.0001%	− 0.0272%	0.00%	0.00%	0.00%
	Difference	1.375×10^{-6}	2.57×10^{-5}	5.37×10^{-15}	-2.30×10^{-7}	-2.75×10^{-5}	-1.693×10^{-12}	1.414×10^{-10}	-7.36×10^{-7}
	Relative change	− 186.8%	− 3480%†	0.00%	31.26%	3740%*	0.00%	0.02%	0.00%

the Glu concentration equals to the background Glu concentration (0 mM). In the table, the term "Change" denotes the difference in concentrations of microforms of each ionic species, $C_{i,z}$, between the peak and baseline: $\Delta C_{i,z} = C_{i,z}$ (peak) -$C_{i,z}$ (baseline). Calculations of the conductivity for microforms are derived from the respective concentration $C_{i,z}$, acid-dissociation constant p$K_{a,i}$, and mobility $\mu_{i,z}$. We used the values stored in Simul 5 for p$K_{a,i}$ and $\mu_{i,z}$. A relative contribution (%) of $\kappa_{i,z}$ to the local conductivity κ for both peak and baseline is also provided. The "Conductivity change" values represent the difference between the peak and baseline conductivities $\Delta\kappa_{i,z} = \kappa_{i,z}$ (peak) -$\kappa_{i,z}$ (baseline) for each microform. Furthermore, the "Relative change" value indicates its relative contribution to the overall conductivity change $\Delta\kappa$, a critical parameter determining the peak height and consequently C4D sensitivity. We present a detailed analysis of ionic contribution to $\Delta\kappa$ in the TRIS/HCl and TRIS/MES buffers. Analysis for the two other buffer systems and associated tables (Tables S4 and S7) is described in Section S.5 of SI.

In the TRIS/HCl buffer (11.56 mM TRIS and 9.54 mM HCl at a neutral pH of 7.4), the concentrations of H^+ and OH^- ions are minimal (~ 10^{-8} to ~ 10^{-7} M, Table 1), contributing negligibly to conductivity κ (<|0.01%|). In contrast, $TRIS^+$ and Cl^- are major ionic species on the order of ~ 10^{-2} M, significantly influencing κ value. However, the two ions exhibited minimum concentration changes from the baseline to the peak (<|0.2%| change). Among Glu^+, Glu^-, and Glu^{2-}, the three ionic microforms of Glu, only Glu^- showed a substantial impact on κ in the peak (~ 10^{-5} vs. ~ 10^{-7} and ~ 10^{-13} S/m for Glu^{2-} and Glu^+, respectively).

Nevertheless, a relative contribution of Glu^- to the peak conductivity κ was still negligible (0.026%) when compared to the ionic constituents of the BGE (27.2% for counter-ion $TRIS^+$ and 72.8% for co-ion Cl^-) due to its low concentration. Remarkably, a relative contribution of the peak-baseline conductivity change ($\Delta\kappa_{i,z}$) of Cl^- to the local peak-baseline conductivity change $\Delta\kappa$ (100%) is most significant (110.7%) compared to those of Glu^- (− 24.6%) and $TRIS^+$ (14.2%). This predominance can be attributed to its superior mobility: 79.1 (Cl^-) vs. 27 (Glu^-) and 29.5×10^{-9} m^2/Vs ($TRIS^+$). The decrease in concentrations of Cl^- and $TRIS^+$ displaced from the peak (-5.256×10^{-6} and -1.525×10^{-5} M, respectively) by increased Glu^- concentration ($+9.946 \times 10^{-6}$ M) and the associated decline in conductivity $\Delta\kappa_{i,z}$ (-1.495×10^{-5} and -1.164×10^{-4} S/m, respectively) are the main factors contributing to the large negative conductivity peak ($\Delta\kappa = -1.052 \times 10^{-4}$ S/m). As TRIS is titrated with HCl at a specific pH of 7.4, the concentration Cl^-, a major ionic species determining $\Delta\kappa$, could vary during the buffer preparation. Therefore, maintaining uniformity in BGE composition and pH is imperative for achieving reliable conductivity detection.

The TRIS/MES buffer composed of 18.2 mM TRIS and 36.4 mM MES maintains a slightly basic pH of 8.1. Consequently, concentrations of H^+ and OH^- are also negligible on the order of 10^{-8} and 10^{-6} M as detailed in Table 2. As a result, these ions have no significant impact on κ (<|0.01%|). Predominant ionic species, $TRIS^+$ and MES^-, exist at much larger concentrations on the order of ~ 10^{-2} M, but their concentrations exhibit negligible changes from the baseline to the peak (<|0.03%| change). Similarly in the TRIS/HCl buffer, only Glu^- microform significantly contributes to κ in the peak (~ 10^{-5} vs. ~ 10^{-6} and ~ 10^{-15} S/m for Glu^{2-} and Glu^+, respectively). Due to its low concentration at pH 8.1, a relative contribution of Glu^- to κ is negligible (0.024%) in contrast to the ionic BGE species (48.7% for MES^- and 51.3% for $TRIS^+$) in the peak. Nonetheless, the relative contribution of peak-baseline conductivity change ($\Delta\kappa_{i,z}$) of Glu^- to the local peak-baseline conductivity change $\Delta\kappa$ (100%) is substantial (-3484.4%), which is comparable to that of MES^- (+3740%) and surpasses that of $TRIS^+$ (+31.26%). Interestingly, the significant increase of $\Delta\kappa_{i,z}$ due to an increase in Glu^- concentration (9.85×10^{-6} M) in the peak was largely offset by a greater decrease in $\Delta\kappa_{i,z}$ for MES^- due to its expulsion from the zone (-1.019×10^{-5} M). This compensation mechanism results in a much smaller negative conductivity peak (-7.36×10^{-7} S/m) compared to that of the TRIS/HCl buffer. Consequently, the MES/TRIS buffer is not ideal for the sensitive detection of Glu because its substantial contribution to negative κ is instantaneously counteracted by MES^--induced conductivity increase.

3.1.3 A Rational Design Guideline for a Background Electrolyte with an Enhanced Sensitivity

From our comprehensive study of the conductivity contributions of ionic species in the model BGEs, several key findings have emerged. First, the choice of BGE species significantly impacts $\Delta\kappa$, the conductivity change between the peak and baseline, and consequently C4D sensitivity. Therefore, careful selection of the BGE, either through experimental or theoretical verification, is crucial. The numerical simulation method presented here can offer a cost- and time-effective alternative to experimental verification. Second, $|\Delta\kappa|$ can be boosted by selecting an appropriate pH where the high-mobility and high-valence microform becomes the major analyte ions, as observed for Glu^{2-} in the TEA/AcOH buffer (Table S7). However, H^+ and OH^- ions, exhibiting significantly higher mobility than those of BGE and analyte ions, should not influence $\Delta\kappa$ significantly. The tested mild pH range (pH 6.1–10.6), selected for our future application (electrophoretic immunoassay in polyacrylamide gel), appears suitable in this regard. Even in the case of the alkaline TEA/AcOH buffer at pH 10.6, which has a relatively

higher OH^- concentration (4.43×10^{-4} M), $\Delta C_{i,z}$, its conductivity change from the baseline to the peak, was minimal (-2.61×10^{-8} M) due to the excellent buffering capacity of the BGE. Therefore, a BGE with an outstanding buffering capacity would be sufficient within this pH range. Third, $\Delta\kappa$ can be enhanced by choosing a higher-mobility BGE co-ion (e.g., Cl^-) and displacing it from the analyte zone, as demonstrated in the TRIS/HCl buffer (Table 1), thereby creating a large negative conductivity peak. Meanwhile, a low-to-medium mobility BGE counter-ion (e.g., $TRIS^+$) should be chosen to minimize the BGE conductivity, ensuring a high SNR. Fourth, unwanted reduction of $|\Delta\kappa|$ can be mitigated by collecting a counter-ion from the neighboring BGE to counteract the displacement of a co-ion from the analyte zone proportional to the analyte concentration, as demonstrated for the MES/His buffer (Table S4). Lastly, it is important to avoid scenarios that increased $|\Delta\kappa|$ caused by the analyte ion is completely nullified by the displaced counter-ions. The TRIS/MES buffer serves as a good example in which the conductivity increases due to the Glu^- peak were counteracted by the displaced MES^- ion with similar mobility and concentration changes, thereby yielding negligible $|\Delta\kappa|$ values (Table 2).

3.1.4 Simulated Dose Response of Conductivity Detection for Glutamic Acid in the Four Background Electrolytes

To predict the slope of conductivity-detection response ($=\Delta\kappa/C$), we varied the concentration of Glu at 0, 10, 20, and 50 µM. Subsequently, we recorded the corresponding conductivity-peak height $\Delta\kappa$ at $t = 60$ s for the four different BGEs. The order of BGEs that yielded slopes from the highest to the lowest was (1) TRIS/HCl, (2) TEA/AcOH, (3) MES/His, and (4) TRIS/MES. This order aligns with the order of $|\Delta\kappa|$ obtained in the study of time- and position-dependent conductivity peaks (Section S.5). Later, the slope predictions were qualitatively compared with the experimental data (see Sect. 3.5 for details).

3.2 Electrophoresis Simulation of Trypsin Inhibitor

3.2.1 Time- and Position-Dependent Concentration of Analyte and Corresponding Conductivity Peak

An electrophoresis simulation of the trypsin inhibitor (TI) was conducted using optimized mesh numbers and time steps, as detailed in Section S.4. A free-solution electrophoresis condition (i.e., no viscous medium) was assumed for this simulation because mobility data of TI in a viscous medium (e.g., 2% 2-hydroxyethyl cellulose) are not readily available in the literature. The other simulation conditions mirrors those used in the Glu simulation. However, there are two major differences. First, only two BGEs, MES/His and MES/TRIS buffers, were tested because TI could not be experimentally detected in the other two buffer systems. Second, the analyte concentration was 24 µM, not 10 µM.

The TI is a 20.1-kDa protein with an isoelectric point of 4.5, comprising 181 AA residues [84]. Its base mobility μ_o is 0.7029×10^{-9} m^2/Vs [85]. Following the software instructions and communications with Gaš' group, we propose an empirical linear equation for the apparent mobility of TI (Eq. S8). This equation is a function of charge number z and, consequently, local pH, serving as a first-degree approximation. Further details about the empirical equation can be found in Section S.3 of SI. Within the pH range of interest, 6.1 for the MES/HIS and 8.1 for the MES/TRIS, the values of z were determined to be -8.31 and -11.5, respectively, according to Simul 5. Consequently, the apparent mobility μ was calculated as 5.84×10^{-9} and 8.08×10^{-9} m^2/Vs. These mobilities are one or two orders of magnitude lower than those of AAs and BGE ions (as indicated in Table S1), implying slower migration for TI.

Figure 5a illustrates the time evolution (0, 60, 120, 180, and 240 s) of the electromigration of TI (black line) and its associated κ (blue line) in the MES/His buffer. The migration of ionized TI was notably slower than that of Glu^- due to its lower mobility (5.84×10^{-9} vs. 27×10^{-9} m^2/Vs). Similar to the Glu electrophoresis case (Fig. 4), the first conductivity peak tracked the migrating TI zone while the second conductivity remained at the injection site. A difference from the Glu simulation was the dispersed TI zone, mainly attributed to electromigration dispersion [59, 61, 62, 66]. Evidence of "peak fronting" (i.e., the peak maximum overtakes the zone's front-end while the zone's tail lags behind) became apparent after $t = 120$ s. This phenomenon suggests that analyte ions are accelerating because the conductivity within the zone is significantly lower than in the neighboring blank BGE and consequently resulting in a higher electric field. Due to the electromigration dispersion, the peak width increased by 10.41%, and height decreased by 1.2% at 240 s, compared to the measurements at 0 s. The electromigration of TI in the TRIS/MES buffer (pH 8.1) shows a comparable outcome with electromigration dispersion (Fig. 5b). Once again, migration of TI was much slower than that of Glu due to a significant difference in their mobility at this specific pH (8.08×10^{-9} vs. 27×10^{-9} m^2/Vs).

3.2.2 Influence of Ionic Concentration and Mobility on Conductivity of Analyte Zone

Using electrophoresis data at $t = 240$ s, we analyzed the contribution of each ionic species to $\Delta\kappa$. The analysis results for the two BGEs are presented in Tables 3 and 4. Given that TI consists of 181 AA residues, it is practically impossible to enumerate all microforms across a wide range of charge numbers ($z = +22$ to -36, corresponding to pH 0 to 14).

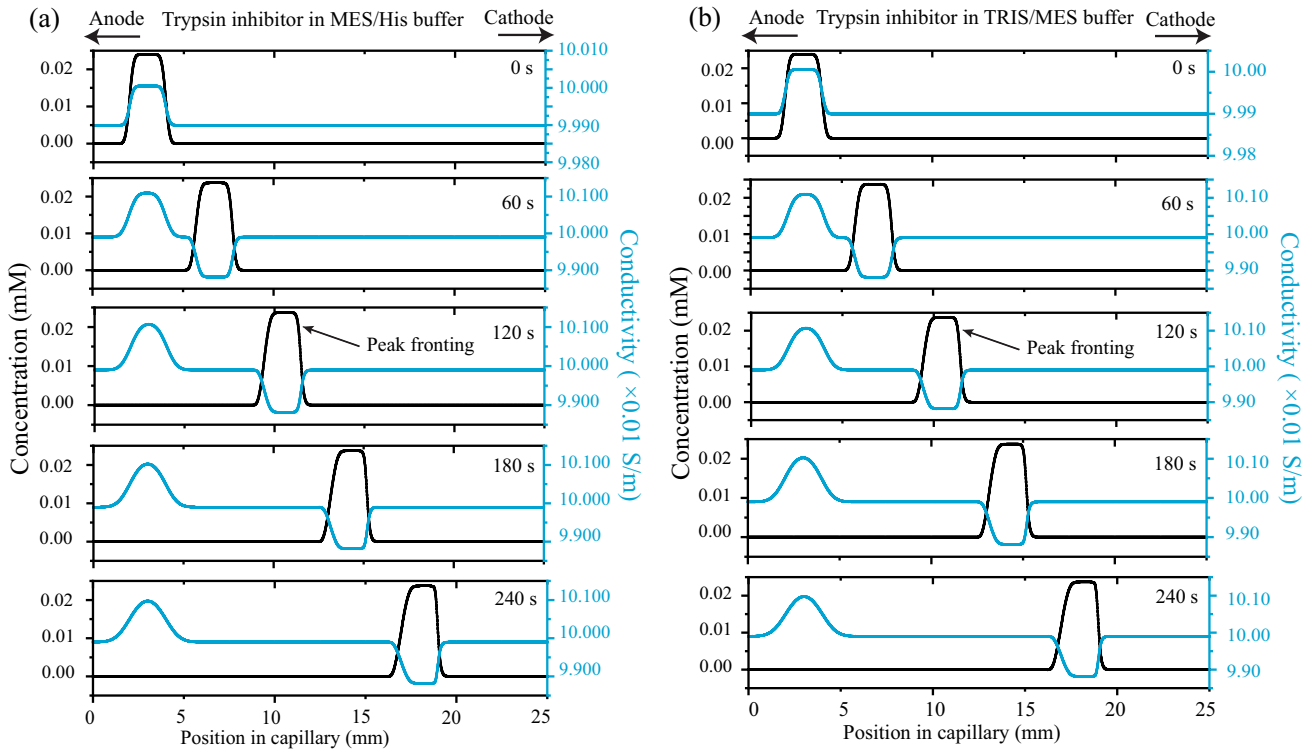

Fig. 5 Time sequences of electrophoresis simulation conducted for trypsin inhibitor (TI) in (**a**) MES/His and (**b**) TRIS/MES buffer. Analyte zones of TI (black line) and co-migrating conductivity peaks (blue line) are depicted for each time step of 0, 15, 30, 45, and 60 s. Both cases exhibited negative conductivity peaks with electromigration dispersion ("peak fronting"). Electrophoresis condition: TI concentration = 24 μM, simulation time = 240 s, capillary length = 25 mm, and separation electric field = 100 V/cm

Table 3 Concentration of microforms of the BGE components, analyte, hydrogen, and hydroxide ions and their contribution to the peak-baseline conductivity change $\Delta\kappa$ for TI electrophoresis simulation in the MES/His buffer at pH 6.1. The concentrations and conductivity are evaluated at the center of the TI zone ("Peak") and background electrolyte ("Baseline")

		Analyte	BGE				H^+/OH^-		
		Ionized TI	MES^-	His^-	His^+	His^{2+}	H^+	OH^-	Total
Concentration (M)	Peak	2.40×10^{-5}	1.855×10^{-2}	1.079×10^{-5}	1.876×10^{-2}	1.653×10^{-6}	8.61×10^{-7}	1.161×10^{-8}	
	Baseline	0.00%	1.888×10^{-2}	1.098×10^{-5}	1.888×10^{-2}	1.655×10^{-6}	8.57×10^{-7}	1.167×10^{-8}	
	Change	2.40×10^{-5}	-3.24×10^{-4}	-1.850×10^{-7}	-1.217×10^{-4}	-1.991×10^{-9}	4.52×10^{-9}	-6.13×10^{-11}	
	Relative change	100.0%	−1.717%	−1.685%	−0.645%	−0.1203%	0.528%	−0.525%	
Conductivity (S/m)	Peak*	1.268×10^{-4}	5.08×10^{-2}	2.95×10^{-5}	4.85×10^{-2}	1.515×10^{-5}	3.01×10^{-5}	2.30×10^{-7}	9.88×10^{-2}
	Peak contribution (%)	0.1284%	50.8%	0.0298%	49.1%	0.0153%	0.0305%	0.000232%	100%
	Baseline	0	5.10×10^{-2}	3.00×10^{-5}	4.88×10^{-2}	1.516×10^{-5}	3.00×10^{-5}	2.31×10^{-7}	9.99×10^{-2}
	Baseline contribution (%)	0.00%	51.1%	0.030%	48.9%	0.01519%	0.030%	0.000231%	100%
	Contribution change (%)	12.84%	−0.336%	−0.0001881%	0.208%	0.000145%	0.000483%	0.0000013%	0.00%
	Difference	1.268×10^{-4}	-8.75×10^{-4}	-5.05×10^{-7}	-3.15×10^{-4}	-1.825×10^{-8}	1.581×10^{-7}	-1.212×10^{-9}	-1.063×10^{-3}
	Relative change	−11.93%	+82.3%	+0.0475%	+29.6%	+0.00172%	−0.01487%	+0.000114%	100%

*TI in the peak: $z = 6.064$ and $\mu = 5.57\times10^{-9}$ m^2/Vs

Table 4 Concentration of microforms of the BGE components, analyte, hydrogen, and hydroxide ions and their contribution to the peak-baseline conductivity change $\Delta\kappa$ for TI electrophoresis simulation in the TRIS/MES buffer at pH 8.1. The concentrations and conductivity are evaluated at the center of the TI zone ("Peak") and background electrolyte ("Baseline")

		Analyte	BGE		H^+/OH^-		
		Ionized TI	$TRIS^+$	MES^-	H^+	OH^-	Total
Concentration (M)	Peak	2.4×10^{-5}	1.765×10^{-2}	1.744×10^{-2}	8.07×10^{-9}	1.239×10^{-6}	
	Baseline	0	1.802×10^{-2}	1.802×10^{-2}	8.23×10^{-9}	1.215×10^{-6}	
	Change	2.4×10^{-5}	-3.59×10^{-4}	-5.69×10^{-4}	-1.604×10^{-10}	2.417×10^{-8}	
	Relative change	100%	−1.992%	−3.157%	−1.951%	1.989%	
Conductivity (S/m)	Peak*	2.05×10^{-4}	5.02×10^{-2}	4.71×10^{-2}	2.82×10^{-7}	2.45×10^{-5}	9.76×10^{-2}
	Peak contribution (%)	0.210%	51.5%	48.3%	0.000289%	0.0251%	100%
	Baseline	0	5.13×10^{-2}	4.87×10^{-2}	2.88×10^{-7}	2.40×10^{-5}	9.99×10^{-2}
	Baseline contribution (%)	0.00%	51.3%	48.7%	0.000288%	0.0240%	100%
	Contribution change (%)	0.210%	0.1893%	−0.401%	0.000001%	0.001069%	0.00%
	Difference	2.05×10^{-4}	-1.021×10^{-3}	-1.536×10^{-3}	-5.61×10^{-9}	4.78×10^{-7}	-2.351×10^{-3}
	Relative change	−8.7331%	+43.40%	+65.3%	+0.000239%	-0.0203%	100%

*TI in the peak: $z=11.6$ and $\mu=8.15\times10^{-9}$ m^2/Vs

Therefore, we established our tables on TI's analytical concentration (Eq. S3) and net charge (the sum of charges of all ionizable AA residues).

In the MES/His buffer (pH of 6.1), H^+ and OH^- were present in negligible concentrations (~ 10^{-6} and ~ 10^{-8} M respectively, Table S4), virtually making no contribution to the local conductivity κ (<|0.04%|). The relative contribution of the ionized TI to κ was also not significant (0.1268%), when compared to those of the major ionic BGE species (50.8% for MES^- and 49.1% for His^+) due to TI's lower concentration and mobilities. However, the relative contribution of TI's $\Delta\kappa_{i,z}$ to $\Delta\kappa$ was not negligible (− 11.93%), when compared to those of MES^- (+82.3%) and His^+ (+29.6%). The charge number of TI was significantly larger than that of Glu (− 8.31 vs. − 0.98) due to its higher concentration (24 vs. 10 µM) and a greater number of AA residues (181 vs. 1). To maintain electroneutrality (Eq. S7) with the higher charge number of TI, concentrations of MES^- and His^+ became much lower in the peak than in the baseline, when compared to the Glu case. TI is collected in the analyte zone ($+2.4\times10^{-5}$ M) while both MES^- and His^+ are displaced from the zone (-3.24×10^{-5} and -1.217×10^{-4} M, respectively). This significant decrease in $\Delta\kappa_{i,z}$ for the faster MES^- and His^+ species ($\mu=28\times10^{-9}$ and 26.8×10^{-9} m^2/Vs, respectively) over the increase of $\Delta\kappa_{i,z}$ for the slower TI species ($\mu=5.84\times10^{-9}$ m^2/Vs) was the primary reason for obtaining an appreciable negative conductivity-peak height $\Delta\kappa$ (-1.063×10^{-3} S/m). This contrasts with the Glu case (Table S4), where Glu^- and His^+ were collected in the analyte zone ($+9.81\times10^{-6}$ and $+2.41\times10^{-6}$ M, respectively) while MES^- is displaced from the zone (-7.40×10^{-6} M). In this instance, a larger increase of $\Delta\kappa_{i,z}$ for Glu^- and His^+ over the reduction of $\Delta\kappa_{i,z}$ for MES^- was the reason for a positive $\Delta\kappa$ ($+1.179\times10^{-5}$ S/m), albeit a much smaller magnitude compared to the TI case.

The results for the TRIS/MES buffer case closely resemble those of the MES/His buffer (Table S4). In this scenario, the conductivity-peak height $\Delta\kappa$ was also negative because an increase in $\Delta\kappa_{i,z}$ due to TI in the analyte zone (2.05×10^{-4} S/m) was overcompensated by a substantial decrease in conductivity attributed to MES^+ (-1.021×10^{-5} S/m) and His^- (-1.536×10^{-4} S/m) ions, displaced by highly-charged TI from the zone (Table 4). Notably, the net charge of TI in the TRIS/MES was higher than that in the MES/His buffer (− 11.5 vs. − 8.31) due to the elevated pH (8.1 vs. 6.1). Consequently, the amounts of displaced co-ion ($\Delta C_{i,z}=-5.69\times10^{-4}$ M vs. -3.24×10^{-4} M for MES^-) and counter-ion ($\Delta C_{i,z}=-3.59\times10^{-4}$ M for $TRIS^+$ vs. -1.217×10^{-4} M for His^+) are larger than those in the MES/His buffer to satisfy the electroneutrality condition. Therefore, the MES/TRIS buffer enables a conductivity measurement of TI that is twice as sensitive as the MES/His buffer ($|\Delta\kappa|=2.35\times10^{-3}$ vs. 1.063×10^{-3} S/m).

It is noteworthy that sensitive conductivity detection of protein can be achieved through a judicious choice of BGE. Conventionally, C4D detection of proteins has been deemed challenging with a typical LOD of µM range, because of their low mobility μ and consequently a small conductivity change $\Delta\kappa_{Ii,z}$. However, some studies demonstrated LODs in nM range for certain proteins [30, 70, 74]. Based on our analysis, proteins with a substantial net charge (a high number of ionizable AA residues) can be detected by displacing BGE co-ion and counter-ion with higher mobility and concentration from the analyte zone. The choice of BGE pH should be such that the protein carries a high net charge, and the concentration of

major BGE microforms (e.g., $TRIS^+$ and MES^-) should significantly outweigh that of minor BGE microforms. This results in a larger effective mobility of BGE species [48]. For example, in the case of the TRIS/MES buffer, every anionic TI replaces approximately 15 $TRIS^+$ and 23.6 MES^- ions, leading to 5 × and 7.4 × reduction in conductivity $\Delta\kappa_{i,z}$ compared to the conductivity increase due to the enriched TI.

3.2.3 Dose Response of Conductivity Detection for Trypsin Inhibitor in Different Background Electrolytes

In order to find a slope of conductivity detection response ($=\Delta\kappa/C$), the concentration of TI was varied (0, 24, 36, 48, and 60 µM), and the corresponding conductivity-peak height $\Delta\kappa$ was recorded at $t = 240$ s for the MES/His and TRIS/MES BGEs. The order of BGEs that yielded slopes, from highest to lowest was (1) TRIS/MES and (2) MES/His. This order aligns with the order of $|\Delta\kappa|$ obtained in the study of time- and position-dependent conductivity peaks (Sect. 3.2.1). Later, the slope predictions were qualitatively compared with the experimental data (see Sect. 3.7 for details).

3.3 Electrophoresis and C4D Detection of Glutamic Acid

Figure 6 displays C4D electropherograms for Glu recorded in the four different BGEs after the separation process has commenced. The peak height increased proportionally with the concentration (10, 20, and 50 µM). The order of peak heights for the same concentration, from highest to lowest, was (1) TRIS/HCl, (2) TEA/AcOH, (3) MES/His, and (4) TRIS/MES buffers. This trend coincides with the simulation results presented in Sect. 3.1.2. Additionally, positive peaks were observed for the MES/His and TEA/AcOH buffers, while negative peaks were observed for the TRIS/HCl and TRIS/MES buffers as observed in the simulation results (Fig. S10). The noisy electropherogram for the TRIS/MES buffer (Fig. 6c) indicates a lower SNR, primarily due to a small conductivity-peak height $\Delta\kappa$, as also predicted from Fig. 4b. Overall, the experimental results exhibited reasonable qualitative agreement with the simulation results.

3.4 Electrophoresis and C4D Detection of Trypsin Inhibitor

The pinched injection method proved ineffective for injecting TI into the separation channel, despite repeated adjustments to voltage programs based on the successful Glu

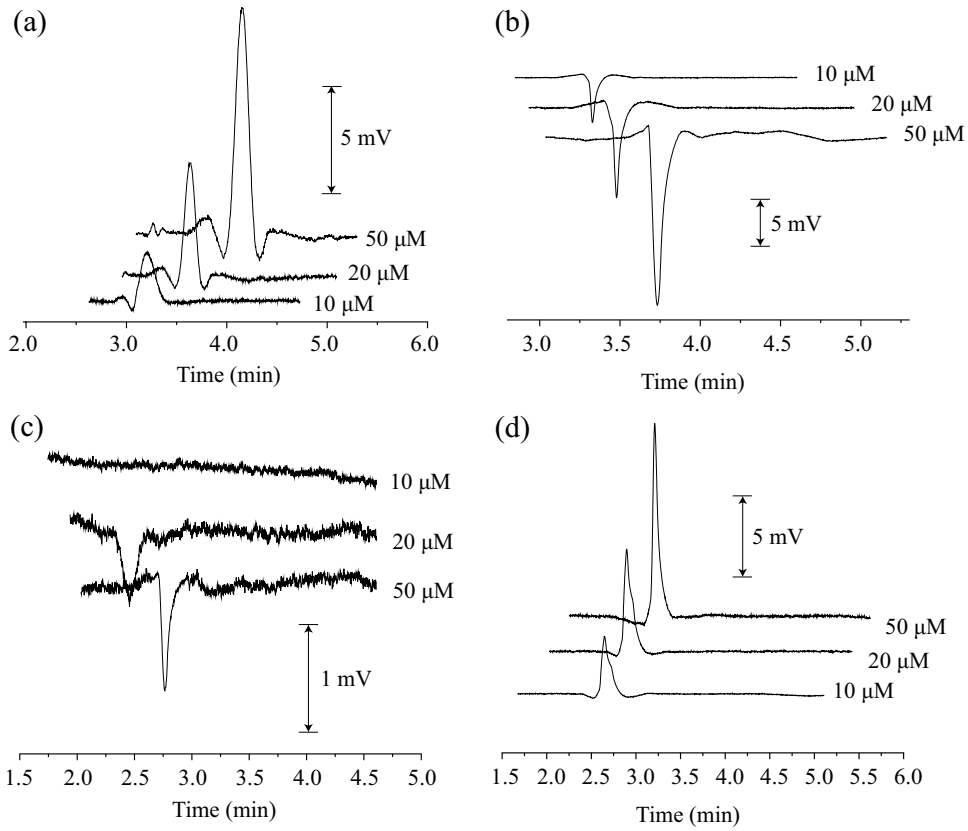

Fig. 6 Electropherogram for glutamic acid (Glu) in (**a**) MES/His buffer (pH 6.1), (**b**) TRIS/HCl buffer (pH 7.4), (**c**) MES/TRIS buffer (pH 8.1), and (**d**) TEA/AcOH buffer (pH 10.6). Experimental condition: Glu concentration = 10, 20, and 50 µM, capillary length = 32.75 mm, loading time = 20 min, loading electric field = 83.14 V/cm, separation electric field = 283.66 V/cm, AC amplitude = 80 V, and AC frequency = 600 kHz

injection and separation. We speculated that the uncontrollable injection was due to unstable EOF, as we observed that the protein band occasionally migrated in the same direction as the applied electric field, contrary to expectations (e.g., negatively charged TI should migrate in the opposite direction of the electric field [86]). To address this problem, a thickening agent of 2% HEC, frequently used to suppress EOF [77, 81], was added to the tested buffers. This modification ultimately enabled the successful loading and separation of TI. However, unstable conductivity signals (i.e., baseline drift and unidentifiable systems peak, Fig. 7) persisted even with the viscous BGE solution, rendering the identification of a TI peak challenging. To address this problem, TI labeled with Alexa Fluor 568 was separated using the same voltage program. Then its conductivity peak was cross-validated using fluorescence imaging and electropherograms (Fig. S2). The degree of labeling (DOL) of Alexa Fluor 568 dyes for TI was close to 1. As a result, its influence on electrophoretic properties such as charge number and mobility was deemed negligible.

C4D detection of the TI was not attainable in all four BGEs. Through cross-validation experiments, we noted that only baseline drift and system peaks were identified in the TRIS/HCl and TEA/AcOH buffer, but not a TI peak. TI peaks were detectable in the MES/His and TRIS/MES buffers (Fig. 7). The peak height increased with an increase in concentration (24, 36, 48, and 60 µM). The conductivity peak of TI in the TRIS/MES buffer exceeded that in the MES/His buffer for the same concentrations. At present, it is unclear why significant baseline drift and system peaks, which were absent in the Glu experiment, are observed in the TI experiment. Some authors attribute these system peaks to various reasons including EOF, complex BGE composition, and extreme pH [87].

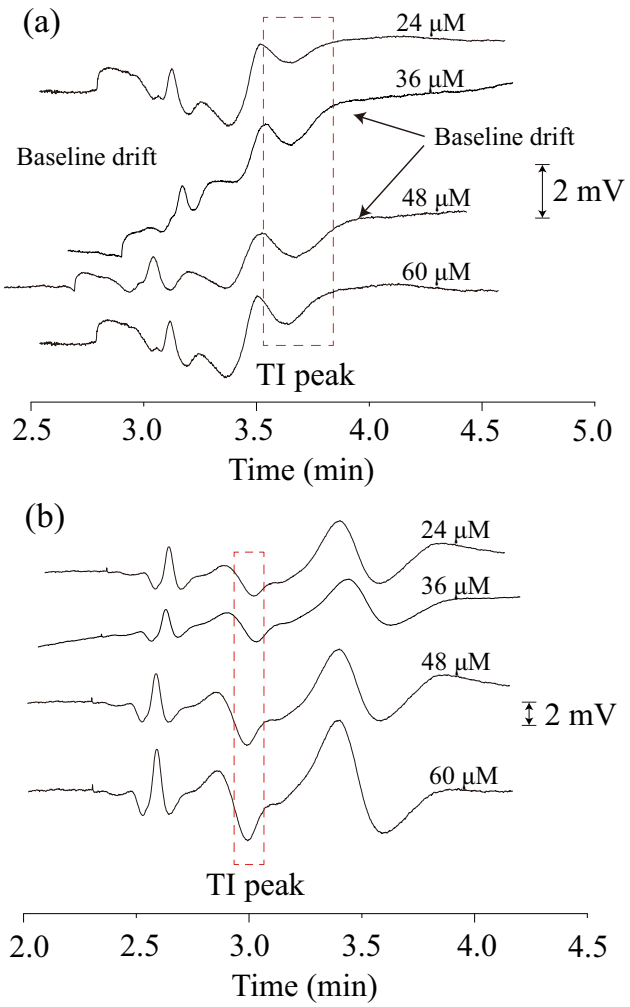

Fig. 7 C4D electropherogram of trypsin inhibitor (TI) in (**a**) the MES/His buffer (pH 6.1) and (**b**) TRIS/MES buffer (pH 8.1), both supplemented with 2% HEC thickening agent. Baseline drift and unidentified systems peaks were observed. The identification of an analyte peak among several systems peaks was confirmed through fluorescence imaging (Fig. S2). The electrophoresis condition is identical to those in Fig. 6 except the C4D parameters: AC amplitude = 160 V and AC frequency = 200 kHz

3.5 Comparison of Numerical Analysis and Experimental Results for Glutamic Acid

In Sect. 3.1 and 3.2, our electrophoresis simulations for the model analytes Glu and TI based on Simul 5, clearly indicate that $|\Delta\kappa|$, the conductivity change between a peak and the baseline, strongly depends on buffer conditions (i.e., acid, base and/or salt species, pH, and ionic strength). The actual electrophoresis and C4D measurement of the same model analytes also confirm the dependency of $|\Delta\kappa|$ on the buffer conditions. Furthermore, we observed a monotonic increase in $|\Delta\kappa|$ with increasing analyte concentrations. In this section, we aim to qualitatively validate the accuracy of our numerical simulations with experimental results.

Figure 8a represents the numerically obtained $\Delta\kappa$ values for Glu at concentrations of 0, 10, 20, and 50 µM. $|\Delta\kappa|$ increased with increasing Glu concentration in a highly linear manner ($R^2 = 0.999$ for all four BGEs). As previously observed in the analysis of $|\Delta\kappa|$ for 10 µM Glu in these buffers (Tables 1, 2, S4, and S7), $|\Delta\kappa|$ was larger in the order of TRIS/HCl, TEA/AcOH, MES/His, and MES/TRIS buffer. The sensitivity, represented by the slope of the dose–response curve, was 1.046×10^{-5}, 2.64×10^{-6}, 1.169×10^{-6}, and 7.28×10^{-8} S/(m µM) for the TRIS/HCl, TEA/AcOH, MES/His, and TRIS/MES buffers, respectively. The reasons for different $|\Delta\kappa|$ values and peak polarities (positive or negative) are explained in detail in Sects. 3.1, 3.2 and S.5.

The experimental results for Glu in the same concentration range exhibited a similar monotonic increase in $|\Delta\kappa|$ as illustrated in Fig. 8b. Furthermore, $|\Delta\kappa|$ followed the

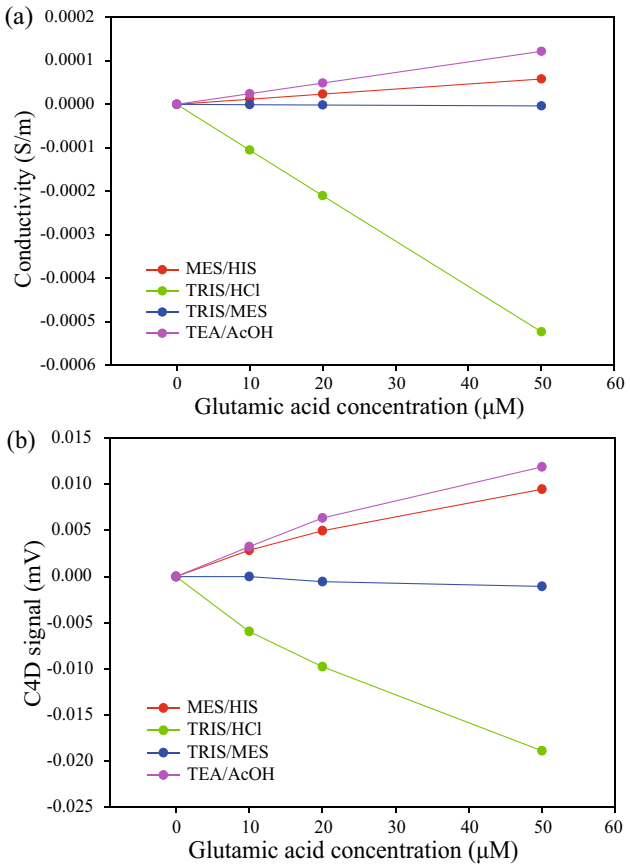

Fig. 8 Relationship between the concentration of glutamic acid (Glu) and the conductivity obtained from (**a**) numerical simulation and (**b**) experimental measurements in the MES/His (pH 6.1), TRIS/HCl (pH 7.4), TRIS/MES (pH 8.1), and TEA/AcOH (pH 10.6) buffers. Both numerical simulation and experimental results qualitatively agree on the order of conductivity change, $|\Delta\kappa|$, in the buffers ranked as TRIS/HCl, TEA/AcOH, MES/His, and TRIS/MES buffers. The relationship exhibits excellent linearity in the simulation data ($R^2 = 0.999$) and slight nonlinearity in the experimental data ($R^2 = 0.946$–0.983). Electrophoresis condition: Glu concentration = 0, 10, 20, and 50 μM; all other conditions are identical to those described in Fig. 6

same order as in the simulation data, ranging from largest to smallest values for the TRIS/HCl, TEA/AcOH, MES/His, and TRIS/MES buffers. However, in contrast to the simulation data (Fig. 8a), the experimental curves demonstrated slight nonlinearity ($R^2 = 0.946$, 0.988, 0.949, 0.973 for the MES/His, TRIS/HCl, TRIS/MES, and TEA/AcOH buffers, respectively). The reasons behind this discrepancy will be provided later in Section 3.8.

It is important to note that the C4D instrument does not measure the absolute conductivity. Instead, it provides relative conductivity expressed in voltage (mV), obtained by multiplying the output AC current with a feedback resistor. Therefore, $|\Delta\kappa|$ obtained from the experiment (in mV) and simulations (in S/m) cannot be compared directly. However, their qualitative trends, depicting the relationship between conductivity and concentration, exhibit a close correspondence, suggesting the effectiveness of our approach in choosing the optimal BGE for achieving the best sensitivity among candidate BGEs.

3.6 Comparison of Conventional Analytical Expressions and Numerical Simulations on Predicting Conductivity-Peak Height

Glu^-, the primary microform of the Glu species in the analyte zone displaces or collects BGE counter-ion or co-ion depending on electrophoretic dynamics (Eq. S1, S2, S5 and S7) and electrophoretic properties including mobility, charge, and concentration. The conductivity-peak height, $\Delta\kappa$, is a result of this complex interplay. Our numerical method can be applied to a partially dissociated, multivalent, multispecies analyte and BGEs without limitations, in contrast to previous approximate analytical expressions [15, 58–60]. However, these mathematical expressions can still provide a first-degree prediction on $|\Delta\kappa|$ and offer an insight into interpreting complex numerical data (Table S.4–S.7) in some limiting cases (see Section S.6 in SI for details). For instance, a simple analytical expression predicts conductivity change $\Delta\kappa$ based on the KRF and electroneutrality condition [58, 83]:

$$\Delta k = c_A \frac{(\mu_A - \mu_S)(\mu_A + \mu_O)}{\mu_A} \frac{F}{10^{-3}K}, \quad (1)$$

where c_A is the concentration of the analyte, F is the Faraday constant, K is the cell constant, and μ_A, μ_S and μ_O are the absolute mobility of the analyte, BGE co-ion, and BGE counter-ion, respectively. This equation was originally formulated for simple monovalent, fully dissociated ions such as the detection of chloride ion in MOPSO/NaOH buffer [58].

From Eq. 1, one can predict an increased conductivity change, and consequently enhanced sensitivity when there is a significant difference between analyte mobility μ_A and BGE co-ion mobility μ_S. For instance, in situations where μ_A greatly exceeds μ_S (e.g., the detection of fast inorganic ion Cl^- in the low-conductivity MES/His buffer), $\Delta\kappa$ is proportional to both μ_A and μ_O (see Eq. S11). However, this condition does not apply to our cases, where the major ionic analyte species Glu^- exhibits low mobility ($\mu_A = 27 \times 10^{-9}$ m^2/Vs), similar to that of BGE co-ions (Table S1). A notable example where the analytical expression (Eq. 1) is relevant is the TRIS/HCl buffer at a neutral pH 7.4. The primary BGE co-ion is Cl^- ($\mu_S = 79.1 \times 10^{-9}$ m^2/Vs), which is replaced by Glu^- with much lower mobility ($\mu_A = 27 \times 10^{-9}$ m^2/Vs). This leads to the largest conductivity change, $|\Delta\kappa|$, when the mobility of the primary BGE counter-ion $TRIS^+$, μ_O ($= 29.5 \times 10^{-9}$ m^2/Vs), is similar to μ_A (as described in Eq.

S13c of SI). These findings are corroborated by the data presented in Table 1 and Fig. 6b. Moreover, the BGE conductivity can also remain suppressed in the TRIS/HCl buffer because μ_O, counter-ion mobility, is still low. Another good example is the TRIS/MES buffer, of which the major co-ion MES^- has a similar mobility to Glu^- ($\mu_A = 27 \times 10^{-9}$ vs. $\mu_S = 28 \times 10^{-9}$ m^2/Vs). In this case, the conductivity change caused by the analyte ion in the zone is offset by that of the displaced co-ion (described in Eq. S12), resulting in the smallest $|\Delta\kappa|$, as evidenced by Table 2 and Fig. 6c. However, Eq. 1 is not easily applicable to the other two BGEs due to the similarity in mobility values, and they are not categorized into any of the limiting cases (Eq. S11–S13). Importantly, it should be reemphasized that Eq. 1 serves as a rough guideline rather than an accurate prediction, primarily because it is only applicable to fully dissociated monovalent ions.

3.7 Comparison of Numerical Analysis and Experimental Results for Trypsin Inhibitor

A similar approach was employed to compare numerical simulations with experimental results for TI. Numerical analyses for TI were conducted in the concentration range of 0, 24, 36, 48, and 60 μM only in the MES/His and MES/TRIS buffers (Sect. 3.2) because no peaks were detectable in the other two buffers. As depicted in Fig. 9a, $|\Delta\kappa|$ increased linearly with increasing TI concentration with a high correlation coefficient of $R^2 = 0.999$ for both buffers. Consistent with our analysis of $\Delta\kappa$ for 24 μM TI in these buffers (see Table 3 and 4), the TRIS/MES buffer exhibited a larger $|\Delta\kappa|$ compared to the MES/His buffer. The slopes of the dose–response curves were -1.018×10^{-4} and -4.82×10^{-5} S/(m μM) for the TRIS/MES and MES/His buffers, respectively. Considering the slope values, one can suggest that TI detection can be performed with nearly 41- and 1398-times higher sensitivity than Glu in the MES/His and TRIS/MES buffers, respectively. For the most sensitive buffers for both analytes, the slope is 9.7 times larger (the TRIS/MES buffer for TI vs. TRIS/HCl for Glu). The reasons for the stronger negative peak are thoroughly explained in Sect. 3.2. Briefly, disproportionally large numbers of co-ionic species (MES^-) and counter-ionic species ($TRIS^+$ or His^+) are displaced from the analyte zone due to the electroneutrality condition and the high charge number of TI, compared to that of Glu (z = -11.5 vs. -1.013 in the TRIS/MES buffer).

The experimental results for TI within the same concentration range also exhibited a monotonic increase in $|\Delta\kappa|$ as illustrated in Fig. 9b. Furthermore, $|\Delta\kappa|$ follows the same order as the simulation results (Fig. 9a). As with the Glu experiments, the dose–response curve exhibited a slight nonlinearity ($R^2 = 0.993$ and 0.996 for the MES/His and TRIS/MES buffers) compared with the simulation results. Similar to the Glu cases, the trends in experimental response align qualitatively with the simulation data. While the simulation suggests 9.7 times more sensitive detection TI than Gu, the experimental slopes for actual C4D detection were 8.4 times lower (TRIS/MES buffer for TI vs. TRIS/HCl for Glu). Additionally, $|\Delta\kappa|$ was not sufficiently large to detect TI in the TRIS/HCl and TEA/AcOH buffers. We speculate that the reason might be a significant reduction in TI mobility in the presence of 2% HEC, which was not accounted for in our simulation. In the next section, we propose possible reasons for the discrepancies between numerical simulation and experimental data as well as less-linear dose–response curves.

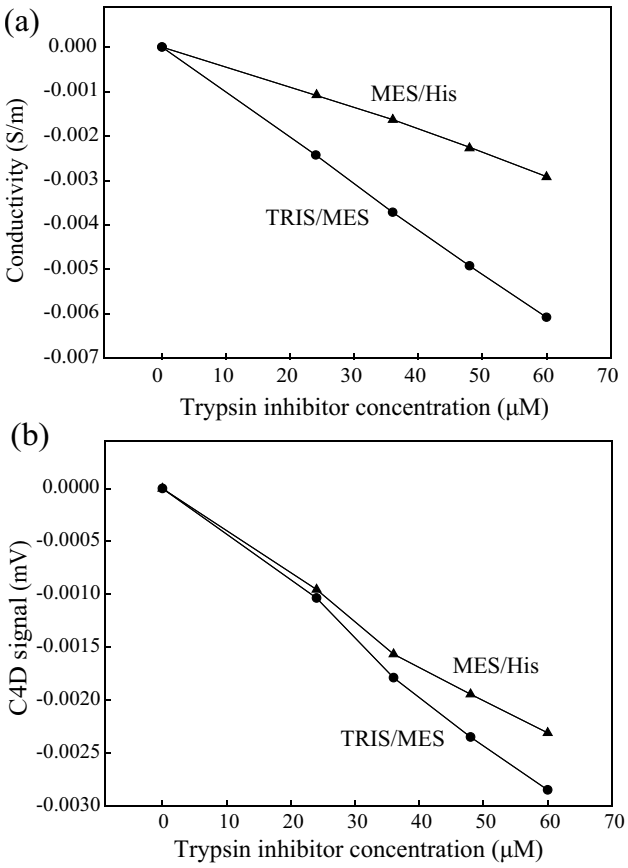

Fig. 9 Relationship between trypsin inhibitor (TI) concentration and conductivity obtained from (**a**) numerical simulation and (**b**) experimental measurements in the MES/His (pH 6.1) and the TRIS/MES (pH 8.1) buffers. Both numerical simulation and experimental results qualitatively agree on the order of conductivity change $|\Delta\kappa|$ in the buffers ranked as the TRIS/MES and MES/His. The relationship exhibited excellent linearity in the simulation data ($R^2 = 0.999$) and slight nonlinearity for the experimental data ($R^2 = 0.993$ and 0.996 for the MES/His and TRIS/MES buffers, respectively). Electrophoresis condition: TI concentration = 0, 24, 36, 48, 60 μM; all other conditions are identical to those described in Fig. 8

3.8 Reasons for Nonlinear Dose Response and Discrepancy Between Simulation and Experiment

We found that the experimental data exhibited less-linear dose responses, compared to the numerical simulation results. The nonlinearity of a C4D system has been a recognized inherent feature since its inception [88]. Several factors contribute to the nonlinearity: (1) The C4D system can be modeled as a characteristic series circuit consisting of a coupling capacitor, a solution resistor, and another coupling capacitor. A high capacitive impedance in this circuit leads to a nonlinear increase in cell admittance with respect to solution conductivity [83]; (2) A stray capacitor runs in parallel with this series circuit and bypasses the excitation signal to the output electrode [83]; and (3) The response of the trans-impedance amplifier is nonlinear [39].

To verify these previous observations, we measured the C4D signal of TRIS/MES conductivity standards in the same C4D setup and microfluidic chip (Fig. 2) within the conductivity range relevant to our work. A clear nonlinear C4D response was observed (Fig. S11 in SI), reaffirming that the nonlinearity is an inherent feature of our C4D system. Mitigating this nonlinearity could be achieved through improvements in detection electronics and careful optimization of operating conditions including operation frequency, excitation voltage, faradaic shielding between the two electrodes, and firm contact of the chip lid with the electrodes, among other considerations.

As mentioned earlier, we performed a qualitative comparison between numerical simulation and experimental results because the absolute conductivity could not be directly measured with the current C4D setup. While both sets of results share an identical order of sensitivity, they differ in terms of absolute conductivity. Instead, we explored whether their relative conductivity, normalized with respect to that of the MES/His buffer, was the same for the experiment and simulation. However, as indicated in Table 5, the relative slopes of the dose–response curve (Fig. 8a and b) for each buffer with respect to that of the MES/His buffer do not match exactly. Only the relative conductivity of the TEA/AcOH buffer shows similarity. For TI, Table 6 provides slopes and relative slopes in the two working buffers, indicating that the relative slopes in the experiment and simulation are different.

Tables 5 and 6 indicates the existence of a non-negligible discrepancy between the simulation and experimental results. We attribute this discrepancy as follows. Firstly, the nonlinearity in conductivity measurement (Fig. S11) could lead to underestimated slopes in the experimental data, contributing to the observed difference. Enhancing the linearity of the C4D system may alleviate this discrepancy. Secondly, the EOF varies among different buffer systems, as we observed, potentially influencing the mobility of ionic species. However, EOF velocity was not accounted for in the numerical simulation. Considering EOF in simulation (an option available in Simul 5) may improve the accuracy of the simulation results, provided that EOF can be reliably measured. Thirdly, inaccurate pK_a values can contribute to the discrepancy. pK_a values influence ionization degree, resulting in inaccurate charge and apparent mobility, and overall accuracy in numerical simulations. For example, a comparison of electrophoresis simulation and experiments for 17 antipsychotic drugs indicated differences in peak height and migration order [56]. It was noted that the inaccuracy of pK_a values was a major source of error, especially when the pH of the BGE is close to the pK_a of the analyte. Therefore, improving the accuracy of electrokinetic parameters including pK_a and mobility may reduce the discrepancy in the future.

Table 5 Slopes and the relative slopes for Glu in four different BGEs obtained from the experiment and simulation

BGE	Experiment		Simulation	
	Slope S/(m μM)	Relative slope	Slope mV/μM	Relative slope
TEA/AcOH	2.87×10^{-4}	2.17	2.64×10^{-6}	2.26
MES/His	1.323×10^{-4}	1.00	1.169×10^{-6}	1.00
TRIS/MES	-2.42×10^{-5}	− 0.183	− 7.27×10⁻8	− 0.0622
TRIS/HCl	-4.08×10^{-4}	− 3.08	− 1.046×10⁻5	− 8.95

Relative slope is obtained by normalizing with that of the MES/His buffer

Table 6 Slopes and the relative slopes for Glu in two different BGEs obtained from the experiment and simulation

BGE	Experiment		Simulation	
	Slope S/(m μM)	Relative slope	Slope mV/μM	Relative slope
MES/His	-3.96×10^{-5}	1.00	-4.82×10^{-5}	1.00
TRIS/MES	-4.88×10^{-5}	1.23	-1.018×10^{-4}	2.11

Relative slope is obtained by normalizing with that of the MES/His buffer

4 Conclusion

The composition of BGE is a crucial factor in MCE systems equipped with a C4D due to its inferior sensitivity compared to fluorescence detection. Therefore, the BGE composition should be optimized to achieve a high C4D sensitivity. We have proposed a Simul 5-based numerical method for designing BGEs to enhance sensitivity. The BGE design process consisting of multiple steps is demonstrated in this work: (1) select model BGEs and analytes, (2) run numerical simulations at test concentrations, (3) analyze contributions of ionic species to conductivity-peak height ($\Delta\kappa$), (4) establish a BGE design guideline for enhanced sensitivity, (5) run numerical simulations with target analytes of varying concentrations, (6) establish the relationship between analyte concentrations and $\Delta\kappa$, (7) select the BGE with the highest sensitivity, and (8) validate simulation results through experimental verification.

We considered four model BGEs, MES/His, TRIS/HCl, TRIS/MES, and TEA/AcOH, previously employed in electrophoresis with C4D detection of AA and proteins. After thoroughly optimizing simulation running conditions, time-dependent electrophoresis simulations for two biochemical analytes, Glu and TI, were conducted. In the simulation results for Glu, the most suitable BGE was TRIS/HCl showing a conductivity-detection sensitivity of -1.046×10^{-5} S/(m μM). This was followed by TEA/AcOH of 2.639×10^{-5} S/(m μM), MES/His of 1.169×10^{-5} S/(m μM), and TRIS/MES of 7.274×10^{-8} S/(m μM). Similar results were obtained in the simulation of TI. The TRIS/MES buffer exhibited a higher detection sensitivity of -1.032×10^{-4} S/(m μM) compared to MES/His of -4.82×10^{-5} S/(m μM). The highest sensitivity in the TRIS/MES buffer was due to the disproportional replacement of co-ionic species $TRIS^+$ and counter-ionic species MES^- by the highly-charged TI protein ($z=-11.5$).

We elucidated the mechanism for positive and negative conductivity peaks by analyzing the contributions of major ionic species in the BGE and analytes to conductivity-detection response $|\Delta\kappa|$. Through this analysis, the following BGE design guideline was derived for improving sensitivity: (1) choosing an appropriate pH where a high-mobility, high-valence microform is the major analyte ion such as for Glu^{2-} in the TEA/AcOH buffer, yet within a range that the concentrations of faster H^+ and OH^- ions in the analyte zone do not strongly influence conductivity; (2) minimizing unwanted reduction of $|\Delta\kappa|$ by collecting a counter-ion from the neighboring BGE to counteract a displaced co-ion from the analyte zone, as demonstrated in the MES/His buffer; (3) replacing a high-mobility BGE counter-ion (e.g., Cl^-) with an analyte ion especially when the mobility of an analyte ion is low or similar to that of a co-ion as shown in the TRIS/HCl buffer. The conductivity detection of AA or protein in low-conductivity BGEs is a good example; lastly, (4) avoiding situations where $|\Delta\kappa|$ increase caused by the analyte ion is completely offset by the displaced counter-ions, as exhibited in the TRIS/MES buffer.

We validated our simulation results by conducting MCE experiments with a C4D detector. We observed excellent qualitative agreement between the order of sensitivity in the simulation and experimental results. However, differences in normalized sensitivity between the simulation results and experimental data were observed. We speculate these discrepancies can be attributed to (1) the inherent nonlinearity of the C4D system, (2) the omission of the EOF in the simulation, (3) inaccuracies of used electrokinetic parameters such as pK_a and mobility of ionic species, and (4) the reduced protein mobility in an EOF-suppressing medium containing 2% HEC (the TI cases).

Despite these limitations, Simul 5 proves to be a valuable tool for predicting $|\Delta\kappa|$, a critical parameter determining the C4D sensitivity, in various BGE systems and providing a BGE design guideline. When the challenges mentioned earlier are properly addressed in the future, numerical simulations with improved accuracy may expedite or even replace the time- and reagent-consuming experimental BGE design processes. Our ongoing efforts aim to improve simulation accuracy, particularly for protein analytes. We anticipate that our work will play a significant role in developing a portable, label-free AA and protein analysis system based on MCE-C4D, by offering a means to enhance detection sensitivity.

Supplementary Information The online version contains supplementary material available at https://doi.org/10.1007/s13206-023-00135-x.

Acknowledgements This work was supported by Basic Science Research Programs through the NRF of Korea funded by the Ministry of Science and ICT (NRF2021R1F1A1045386 and NRF-2022R1A2C1002729).

Data availability Not applicable.

Declarations

Conflict of interest The authors declare that they have no conflict of interest.

References

1. Castro, E.R., Manz, A.: Present state of microchip electrophoresis: State of the art and routine applications. J. Chromatogr. A **1382**, 66–85 (2015)
2. Dittrich, P.S., Manz, A.: Lab-on-a-chip: microfluidics in drug discovery. Nat. Rev. Drug Discov. **5**, 210–218 (2006)
3. Tůma, P.: Determination of amino acids by capillary and microchip electrophoresis with contactless conductivity detection

– Theory, instrumentation and applications. Talanta **224**, 121922 (2021)
4. Gomez, F.J.V., Silva, M.F.: Microchip electrophoresis for wine analysis. Anal. Bioanal. Chem. **408**, 8643–8653 (2016)
5. Wang, R., Wang, X.: Sensing of inorganic ions in microfluidic devices. Sens. Actuators B Chem. **329**, 129171 (2021)
6. Nouwairi, R.L., O'Connell, K.C., Gunnoe, L.M., Landers, J.P.: Microchip electrophoresis for fluorescence-based measurement of polynucleic acids: recent developments. Anal. Chem. **93**, 367–387 (2021)
7. Ou, G., Feng, X., Du, W., Liu, X., Liu, B.-F.: Recent advances in microchip electrophoresis for amino acid analysis. Anal. Bioanal. Chem. **405**, 7907–7918 (2013)
8. Kašička, V.: Recent developments in capillary and microchip electroseparations of peptides (2013–middle 2015). Electrophoresis **37**, 162–188 (2016)
9. Dawod, M., Arvin, N.E., Kennedy, R.T.: Recent advances in protein analysis by capillary and microchip electrophoresis. Analyst **142**, 1847–1866 (2017)
10. Stanisavljevic, M., Vaculovicova, M., Kizek, R., Adam, V.: Capillary electrophoresis of quantum dots: Minireview. Electrophoresis **35**, 1929–1937 (2014)
11. Kitagawa, F., Otsuka, K.: Micellar electrokinetic chromatography on microchips. J. Sep. Sci. **31**, 794–802 (2008)
12. Kawai, T.: Recent advances in trace bioanalysis by capillary electrophoresis. Anal. Sci. **37**, 27–36 (2021)
13. Craig, D.B., Dovichi, N.J.: Multiple labeling of proteins. Anal. Chem. **70**, 2493–2494 (1998)
14. Chau, M.K., Arega, N.G., Nhung Tran, N.A., Song, J., Lee, S., Kim, J., Chung, M., Kim, D.: Capacitively coupled contactless conductivity detection for microfluidic capillary isoelectric focusing. Anal. Chim. Acta **1124**, 60–70 (2020)
15. Zemann, A.J.: Conductivity detection in capillary electrophoresis. Trends Anal. Chem. **20**, 346–354 (2001)
16. Šolínová, V., Kašička, V.: Recent applications of conductivity detection in capillary and chip electrophoresis. J. Sep. Sci. **29**, 1743–1762 (2006)
17. Angeline, N., Choo, S.-S., Kim, C.-H., Bhang, S.H., Kim, T.-H.: Precise electrical detection of curcumin cytotoxicity in human liver cancer cells. Biochip J. **15**, 52–60 (2021)
18. Assaifan, A.K., Alqahtani, F.A., Alnamlah, S., Almutairi, R., Alkhammash, H.I.: Detection and real-time monitoring of LDL-cholesterol by redox-free impedimetric biosensors. Biochip J. **16**, 197–206 (2022)
19. Kim, B., Yao, W., Rhie, J.W., Chun, H.: Microfluidic potentiometric cytometry for size-selective micro dispersion analysis. Biochip J. **16**, 471–479 (2022)
20. Tieu, M.-V., Pham, D.T., Le, H.T.N., Hoang, T.X. Cho, S.: Rapid and ultrasensitive detection of Staphylococcus aureus using a gold-interdigitated single-wave-shaped electrode (Au-ISWE) electrochemical biosensor. Biochip J. (2023). https://doi.org/10.1007/s13206-023-00126-y
21. Drevinskas, T., Maruška, A., Briedis, V.: Capacitance-to-digital: The upgrades of single chip detector. Electrophoresis **36**, 292–297 (2015)
22. Hauser, P.C., Kubáň, P.: Capacitively coupled contactless conductivity detection for analytical techniques – Developments from 2018 to 2020. J. Chromatogr. A **1632**, 461616 (2020)
23. Sierra, T., Crevillen, A.G., Escarpa, A.: Electrochemical detection based on nanomaterials in CE and microfluidic systems. Electrophoresis **40**, 113–123 (2019)
24. Pumera, M., Wang, J., Opekar, F., Jelínek, I., Feldman, J., Löwe, H., Hardt, S.: Contactless conductivity detector for microchip capillary electrophoresis. Anal. Chem. **74**, 1968–1971 (2002)
25. Pumera, M.: Contactless conductivity detection for microfluidics: Designs and applications. Talanta **74**, 358–364 (2007)
26. Zemann, A.J., Schnell, E., Volgger, D., Bonn, G.K.: Contactless conductivity detection for capillary electrophoresis. Anal. Chem. **70**, 563–567 (1998)
27. Tůma, P.: Monitoring of biologically active substances in clinical samples by capillary and microchip electrophoresis with contactless conductivity detection: A review. Anal. Chim. Acta **1225**, 340161 (2022)
28. Wang, J., Chen, G., Chatrathi, M.P., Wang, M., Rinehart, R., Muck, A.: Screen-printed contactless conductivity detector for microchip capillary electrophoresis. Electroanalysis **20**, 2416–2421 (2008)
29. Wang, J., Liu, Y., He, W., Chen, Y., You, H.: A novel planar grounded capacitively coupled contactless conductivity detector for microchip electrophoresis. Micromachines **13**, 394 (2022)
30. Abad-Villar, E.M., Kubáň, P., Hauser, P.C.: Determination of biochemical species on electrophoresis chips with an external contactless conductivity detector. Electrophoresis **26**, 3609–3614 (2005)
31. Wan, Q.J., Kubáň, P., Tanyanyiwa, J., Rainelli, A., Hauser, P.C.: Determination of major inorganic ions in blood serum and urine by capillary electrophoresis with contactless conductivity detection. Anal. Chim. Acta **525**, 11–16 (2004)
32. Tanyanyiwa, J., Abad-Villar, E.M., Hauser, P.C.: Contactless conductivity detection of selected organic ions in on-chip electrophoresis. Electrophoresis **25**, 903–908 (2004)
33. Gong, X.Y., Dobrunz, D., Kümin, M., Wiesner, M., Revell, J.D., Wennemers, H., Hauser, P.C.: Separating stereoisomers of di-, tri-, and tetrapeptides using capillary electrophoresis with contactless conductivity detection. J. Sep. Sci. **31**, 565–573 (2008)
34. Ma, L.-B., Xu, Y., Liang, J., Liu, H.-T., Gan, J., Li, D.-S., Peng, J.-L., Wu, S.: Separation and detection of urinary proteins by microfluidic chip integrated with contactless conductivity detector. Chinese J. Anal. Chem. **39**, 1123–1127 (2011)
35. Fang, X., Zhang, H., Zhang, F., Jing, F., Mao, H., Jin, Q., Zhao, J.: Real-time monitoring of strand-displacement DNA amplification by a contactless electrochemical microsystem using interdigitated electrodes. Lab Chip **12**, 3190–3196 (2012)
36. Emaminejad, S., Javanmard, M., Dutton, R.W., Davis, R.W.: Microfluidic diagnostic tool for the developing world: contactless impedance flow cytometry. Lab Chip **12**, 4499–4507 (2012)
37. Duarte, L.C., Chagas, C.L.S., Ribeiro, L.E.B., Coltro, W.K.T.: 3D printing of microfluidic devices with embedded sensing electrodes for generating and measuring the size of microdroplets based on contactless conductivity detection. Sens. Actuators B Chem. **251**, 427–432 (2017)
38. Cheng, Y.-F., Dovichi, N.J.: Subattomole amino acid analysis by capillary zone electrophoresis and laser-induced fluorescence. Science **242**, 562–564 (1988)
39. Brito-Neto, J.G.A., Fracassi da Silva, J.A., Blanes, L. do Lago, C.L.: Understanding capacitively coupled contactless conductivity detection in capillary and microchip electrophoresis. Part 2. Peak shape, stray capacitance, noise, and actual electronics. Electroanalysis **17**, 1207–1214 (2005)
40. Wang, Y., Cao, X., Hogan, A., Messina, W. Moore, E.J. Fabrication of a grounded electrodes cell with capacitively coupled contactless conductivity detection technique in a microchip capillary electrophoresis application. In: 2018 IEEE 18th International Conference on Nanotechnology, 1–4 (2018)
41. Mahabadi, K.A., Rodriguez, I., Lim, C.Y., Maurya, D.K., de Hauser, P.C., Rooij, N.F.: Capacitively coupled contactless conductivity detection with dual top–bottom cell configuration for microchip electrophoresis. Electrophoresis **31**, 1063–1070 (2010)
42. Huck, C., Poghossian, A., Bäcker, M., Chaudhuri, S., Zander, W., Schubert, J., Begoyan, V.K., Buniatyan, V.V., Wagner, P., Schöning, M.J.: Capacitively coupled electrolyte-conductivity

sensor based on high-k material of barium strontium titanate. Sens. Actuators B Chem. **198**, 102–109 (2014)
43. Ansari, K., Ying, J.Y.S., Hauser, P.C., de Rooij, N.F., Rodriguez, I.: A portable lab-on-a-chip instrument based on MCE with dual top–bottom capacitive coupled contactless conductivity detector in replaceable cell cartridge. Electrophoresis **34**, 1390–1399 (2013)
44. Kubáň, P., Hauser, P.C.: Effects of the cell geometry and operating parameters on the performance of an external contactless conductivity detector for microchip electrophoresis. Lab Chip **5**, 407–415 (2005)
45. Lichtenberg, J., de Rooij, N.F., Verpoorte, E.: A microchip electrophoresis system with integrated in-plane electrodes for contactless conductivity detection. Electrophoresis **23**, 3769–3780 (2002)
46. Cong, Y., Bottenus, D., Liu, B., Clark, S.B., Ivory, C.F.: ITP of lanthanides in microfluidic PMMA chip. Electrophoresis **35**, 646–653 (2014)
47. Kok, W.: The background electrolyte, In: Berger, T.A., Engelhardt H. (eds.) Capillary Electrophoresis: Instrumentation and Operation, pp. 36–43. Vieweg Publishing, Wiesbaden (2000)
48. Persat, A., Suss, M.E., Santiago, J.G.: Basic principles of electrolyte chemistry for microfluidic electrokinetics. Part II: Coupling between ion mobility, electrolysis, and acid–base equilibria. Lab Chip **9**, 2454–2469 (2009)
49. Beckers, J.L., Boček, P.: The preparation of background electrolytes in capillary zone electrophoresis: Golden rules and pitfalls. Electrophoresis **24**, 518–535 (2003)
50. Thredgold, L.D., Ellis, A.V., Lenehan, C.E.: Direct detection of histamine in fish flesh using microchip electrophoresis with capacitively coupled contactless conductivity detection. Anal. Methods **7**, 1802–1808 (2015)
51. El-Attug, M.N., Hoogmartens, J., Adams, E.V., Schepdael, A.: Optimization of capillary electrophoresis method with contactless conductivity detection for the analysis of tobramycin and its related substances. J. Pharm. Biomed. Anal. **58**, 49–57 (2012)
52. Doseděl̆ová, V., Ďurč, P., Dolina, J., Konečný, Š, Foret, F., Kubáň, P.: Analysis of bicarbonate, phosphate and other anions in saliva by capillary electrophoresis with capacitively coupled contactless conductivity detection in diagnostics of gastroesophageal reflux disease. Electrophoresis **41**, 116–122 (2020)
53. Lačná, J., Přikryl, J., Teshima, N., Murakami, H., Esaka, Y., Foret, F., Kubáň, P.: Optimization of background electrolyte composition for simultaneous contactless conductivity and fluorescence detection in capillary electrophoresis of biological samples. Electrophoresis **40**, 2390–2397 (2019)
54. Coufal, P., Zuska, J., van de Goor, T., Smith, V., Gaš, B.: Separation of twenty underivatized essential amino acids by capillary zone electrophoresis with contactless conductivity detection. Electrophoresis **24**, 671–677 (2003)
55. Samcová, E., Tůma, P.: Determination of proteinogenic amino acids in human plasma by capillary electrophoresis with contactless conductivity detection. Electroanalysis **18**, 152–157 (2006)
56. Johns, K.F., Breadmore, M.C., Bruno, R., Haddad, P.R.: Evaluation of PeakMaster for computer-aided multivariate optimisation of a CE separation of 17 antipsychotic drugs using minimal experimental data. Electrophoresis **30**, 839–847 (2009)
57. Bier, M., Palusinski, O.A., Mosher, R.A., Saville, D.A.: Electrophoresis: Mathematical modeling and computer simulation. Science **219**, 1281–1287 (1983)
58. Katzmayr, M.U., Klampfl, C.W., Buchberger, W.: Optimization of conductivity detection of low-molecular-mass anions in capillary zone electrophoresis. J. Chromatogr. A **850**, 355–362 (1999)
59. Jaroš, M., Soga, T., van de Goor, T., Gaš, B.: Conductivity detection in capillary zone electrophoresis: Inspection by PeakMaster. Electrophoresis **26**, 1948–1953 (2005)
60. Gaš, B., Coufal, P., Jaroš, M., Muzikář, J. Jelínek, I.: Optimization of background electrolytes for capillary electrophoresis: I. Mathematical and computational model. J. Chromatogr. A **905**, 269–279 (2001)
61. Jaroš, M., Včeláková, K., Zusková, I., Gaš, B.: Optimization of background electrolytes for capillary electrophoresis: II. Computer simulation and comparison with experiments. Electrophoresis **23**, 2667–2677 (2002)
62. Riesová, M., Hruška, V., Gaš, B.: A nonlinear electrophoretic model for PeakMaster: II. Experimental verification. Electrophoresis **33**, 931–937 (2012)
63. Hruška, V., Jaroš, M., Gaš, B.: Simul 5 – Free dynamic simulator of electrophoresis. Electrophoresis **27**, 984–991 (2006)
64. Bercovici, M., Lele, S.K., Santiago, J.G.: Open source simulation tool for electrophoretic stacking, focusing, and separation. J. Chromatogr. A **1216**, 1008–1018 (2009)
65. Thormann, W., Mosher, R.A.: Dynamic computer simulations of electrophoresis: 2010–2020. Electrophoresis **43**, 10–36 (2022)
66. Gaš, B.: PeakMaster and Simul – Software tools for mastering electrophoresis. Trends Anal. Chem. **165**, 117134 (2023)
67. Smejkal, P., Bottenus, D., Breadmore, M.C., Guijt, R.M., Ivory, C.F., Foret, F., Macka, M.: Microfluidic isotachophoresis: A review. Electrophoresis **34**, 1493–1509 (2013)
68. Malý, M., Dovhunová, M., Dvořák, M., Gerlero, G.S., Kler, P.A., Hruška, V., Dubský, P.: Generalized model of the linear theory of electromigration and its application to electrokinetic chromatography: Theory and software PeakMaster 6—Next Generation. Electrophoresis **40**, 683–692 (2019)
69. Zhou, Y., Danbolt, N.C.: Glutamate as a neurotransmitter in the healthy brain. J. Neural Transm. **121**, 799–817 (2014)
70. Abad-Villar, E.M., Tanyanyiwa, J., Fernández-Abedul, M.T., Costa-García, A., Hauser, P.C.: Detection of human immunoglobulin in microchip and conventional capillary electrophoresis with contactless conductivity measurements. Anal. Chem. **76**, 1282–1288 (2004)
71. Mai, T.D., d'Orlyé, F., Varenne, A.: A comprehensive study of silanization and co-condensation for straightforward single-step covalent neutral capillary coating. Chromatographia **78**, 775–783 (2015)
72. Abad-Villar, E.M., Kubán, P. Hauser, P.C.: Evaluation of the detection of biomolecules in capillary electrophoresis by contactless conductivity measurement. J. Sep. Sci. **29**, 1031–1037 (2006)
73. Knjazeva, T., Kulp, M., Kaljurand, M.: CE separation of various analytes of biological origin using polyether ether ketone capillaries and contactless conductivity detection. Electrophoresis **30**, 424–430 (2009)
74. Tursen, J., Wang, A., Qin, W.: Electrophoretic separation of acidic and basic proteins in the presence of micromolar concentrations of an ionic liquid. Microchim. Acta **174**, 63–71 (2011)
75. Chen, T., Lee, T.-R., Liang, W.-G., Chang, W.-S.W., Lyu, P.-C.: Identification of trypsin-inhibitory site and structure determination of human SPINK2 serine proteinase inhibitor. Proteins **77**, 209–219 (2009)
76. Kim, D., Karns, K., Tia, S.Q., He, M., Herr, A.E.: Electrostatic protein immobilization using charged polyacrylamide gels and cationic detergent microfluidic western blotting. Anal. Chem. **84**, 2533–2540 (2012)
77. Arega, N.G., Heard, W.N., Tran, N.A.N., Jung, S., Meng, J., Chung, M., Kim, M.-S., Kim, D.: Zinc-finger-protein-based microfluidic electrophoretic mobility reversal assay for quantitative double-stranded DNA analysis. Biochip J. **15**, 381–395 (2021)
78. Duong, H.A., Vu, M.T., Nguyen, T.D., Nguyen, M.H., Mai, T.D.: Determination of 10-hydroxy-2-decenoic acid and free amino acids in royal jelly supplements with purpose-made capillary electrophoresis coupled with contactless conductivity detection. J. Food Compost. Anal. **87**, 103422 (2020)

79. Cappelini, L.T.D., de Fátima Menegoci Eugênio, P., Leão, P.A.G.C., Alberice, J.V., Urbaczek, A.C., Assunção, N.A., Juliano, L. Carrilho, E.: Capillary electrophoresis coupled to contactless conductivity detection for analysis of amino acids of agricultural interest in composting. Electrophoresis **37**, 2449–2457 (2016)
80. Reverberi, R., Reverberi, L.: Factors affecting the antigen-antibody reaction. Blood Transfus. **5**, 227–240 (2007)
81. Chung, M., Kim, D., Herr, A.E.: Polymer sieving matrices in microanalytical electrophoresis. Analyst **139**, 5635–5654 (2014)
82. Bottenus, D., Jubery, T.Z., Dutta, P., Ivory, C.F.: 10 000-fold concentration increase in proteins in a cascade microchip using anionic ITP by a 3-D numerical simulation with experimental results. Electrophoresis **32**, 550–562 (2011)
83. Brito-Neto, J.G.A., Fracassi da Silva, J.A., Blanes, L. do Lago, C.L.: Understanding capacitively coupled contactless conductivity detection in capillary and microchip electrophoresis. Part 1. Fundamentals. Electroanalysis **17**, 1198–1206 (2005)
84. Koide, T., Tsunasawa, S., Ikenaka, T.: The amino acid sequence of soybean trypsin inhibitor (Kunitz). J. Biochem. **71**, 165–167 (1972)
85. Rackis, J.J.: Soybean trypsin inhibitors: isolation, purification and physical properties. Arch. Biochem. Biophys. **98,** 471–478 (1962)
86. Ghosal, S.: Effect of analyte adsorption on the electroosmotic flow in microfluidic channels. Anal. Chem. **74**, 771–775 (2002)
87. Sursyakova, V.V., Kalyakin, S.N., Burmakina, G.V., Rubaylo, A.I.: System peaks in capillary zone electrophoresis of anions with negative voltage polarity and counter-electroosmotic flow. Electrophoresis **32**, 210–217 (2011)
88. Ji, H., Lyu, Y., Wang, B., Huang, Z., Li, H., Yan, Y.: An improved capacitively coupled contactless conductivity detection sensor for industrial applications. Sens. Actuators A Phys. **235**, 273–280 (2015)